



Geochemistry, Geophysics, Geosystems

RESEARCH ARTICLE

10.1029/2020GC009413

Key Points:

- We explore the impacts of unmodeled relief and crustal heterogeneity on coseismic deformation and inversions for fault geometry and slip for the Gorkha earthquake
- Excluding relief and crustal heterogeneity biases the determination of fault depth and dip, respectively
- Inverted fault slip distribution trades off significantly with fault depth and dip angle, regardless of the presence of relief and/or crustal heterogeneity

Supporting Information:

Supporting Information S1

Correspondence to:

S. Li, shaoyangli@eri.u-tokyo.ac.jp

Citation:

Li, S., & Barnhart, W. D. (2020). Impacts of topographic relief and crustal heterogeneity on coseismic deformation and inversions for fault geometry and slip: A case study of the 2015 Gorkha earthquake in the central Himalayan arc. *Geochemistry, Geophysics, Geosystems, 21*, e2020GC009413. https://doi.org/10.1029/2020GC009413

Received 2 SEP 2020 Accepted 6 NOV 2020

© 2020. American Geophysical Union. All Rights Reserved.

Impacts of Topographic Relief and Crustal Heterogeneity on Coseismic Deformation and Inversions for Fault Geometry and Slip: A Case Study of the 2015 Gorkha Earthquake in the Central Himalayan Arc

Shaoyang Li¹, and William D. Barnhart²

¹Earthquake Research Institute, The University of Tokyo, Tokyo, Japan, ²Department of Earth and Environmental Sciences, The University of Iowa, Iowa City, IA, USA

Abstract Fault source models inverted from surface displacement measurements are a common tool to contextualize the seismotectonic significance of earthquakes. However, these models commonly invoke a simplified homogeneous elastic half-space (flat Earth) description of Earth, which may bias the resulting fault geometries and slip distributions in the presence of spatially varying Earth's elastic structure and topography. Here, we developed both forward and inverse three-dimensional finite-element models with planar faults to systematically assess the impacts of topography, crustal elastic structure, and fault geometry on surface deformation and earthquake source inversions, with a focus on the 2015 Gorkha, Nepal earthquake. Our forward models with fixed fault slip confirm the impacts of topography and crustal heterogeneity on surface deformation. These impacts, however, contribute only maximally ~10% of the total surface displacement, and the fault depth and dip dominantly control the coseismic deformation for the Gorkha case. When using homogeneous half-space models to invert the synthetic displacement fields generated by forward finite-element models, we find that ignoring crustal heterogeneity primarily biases inferred dip angle, while ignoring relief primarily biases inferred fault depth. Our inversions based on finite-element models suggest that topography and crustal heterogeneity introduce negligible bias on recovering the Gorkha line of sight observations. Fault dip angle and depth can systematically trade off with slip area and slip magnitude, regardless of the presence of relief and crustal heterogeneities. Taken together, our findings highlight the importance of fault geometry on inverted fault kinematics with geodetic observations in the central Himalayan arc.

1. Introduction

In the past decades, space-based geodetic systems, in particular Global Positioning System (GPS) and interferometric synthetic aperture radar (InSAR), have revolutionized our ability to monitor actively deforming areas with unprecedented spatial and temporal resolutions, revealing a wide spectrum of deformation processes that related to active tectonics on Earth (Bürgmann & Thatcher, 2013). Modeling of these geodetic observations has provided further insights into the fault kinematics and rheological structure at largescale fault systems in the different stages of earthquake cycle (e.g., Arnadóttir & Segall, 1994; Bürgmann & Dresen, 2008; Fialko, 2006; Freed et al., 2017; Hearn & Bürgmann, 2005; Itoh et al., 2019; Li et al., 2015; Li, Bedford et al., 2018; Pollitz, 2015; Qiu et al., 2018; Sato et al., 2010; T. Sun & Wang, 2015; K. Wang et al., 2012; Zhao et al., 2017). For the coseismic stage, surface deformation has been used to invert for the fault geometry (including its depth, strike, and dip angles) and slip distribution (i.e., earthquake source) of earthquakes at depth (e.g., Arnadóttir & Segall, 1994; Clarke et al., 1997; Reilinger et al., 2000; Simons et al., 2002). These inversions are particularly useful to routinely document the earthquake kinematics located in inaccessible regions, to independently constrain earthquake impact products (e.g., Barnhart et al., 2019) and to initiate investigations of subsequent postseismic deformation transients (e.g., Pollitz et al., 2001). Most frequently, these inversions invoke computationally efficient solutions for deformation due to dislocations in an elastically homogeneous half-space with a flat Earth surface (no topographic relief) (e.g., Okada, 1985). Many previous studies have used linear or nonlinear sampling techniques (e.g., grid-searching, Monte Carlo, Markov chain Monte Carlo, Neighborhood Algorithm) to invert the earthquake source in a homogeneous or layered flat Earth with analytical or semianalytical solutions, which

LI AND BARNHART 1 of 25



can explain reasonably well the geodetic observations (e.g., Arnadóttir & Segall, 1994; Barnhart et al., 2015; Clarke et al., 1997; Duputel et al., 2014; Fialko, 2004; Fukahata & Wright, 2008; Fukuda & Johnson, 2008; Funning et al., 2007; Hsu et al., 2011; Ragon et al., 2018; Sambridge, 1999; Stramondo et al., 2005; J. Sun et al., 2011; Wright et al., 1999).

Recent increases in the quantity and quality of space-based geodetic observations (Bürgmann & Thatcher, 2013) and ongoing advances of numerical tools and computational capability have permitted further exploration of epistemic uncertainty of the earthquake source model that considers more realistic and detailed Earth structure and/or surface topography. Recent works have emphasized the impacts of including heterogeneous Earth structure and/or surface topography on surface deformation and inversions for fault slip distribution and confirmed the sensitivity of inversion results on these model complexities (e.g., Fialko, 2004; Hashima et al., 2016; Hearn & Bürgmann, 2005; Hsu et al., 2011; Kyriakopoulos et al., 2013; Langer et al., 2019; Langer et al., 2020; Masterlark, 2003; Masterlark et al., 2001; Pollitz, 1996; Sato et al., 2007; Simons et al., 2002; Tung & Masterlark, 2016; R. Wang et al., 2003; K. Wang & Fialko, 2018; Williams & Wallace, 2015; Zhang et al., 2019). The conclusions of different case studies are oftentimes different and even opposite: some suggest that including crustal heterogeneities in their models improves the recovery of geodetic data at a high confidence level (e.g., Tung & Masterlark, 2016; Zhang et al., 2019), while others find no or insignificant improvements of data recovery (e.g., Hashima et al., 2016; Hsu et al., 2011; Simons et al., 2002; K. Wang & Fialko, 2018); some conclude the contribution of topographic relief on surface deformation is in particular considerable (e.g., Hsu et al., 2011; Langer et al., 2019), while others consider such a contribution to be minor (e.g., K. Wang & Fialko, 2018; Zhang et al., 2019). An important issue that potentially influenced such conclusions is that these previous studies commonly inverted for the slip distribution without systematically considering the possible variety of fault geometry in the presence of topographic relief and/or crustal heterogeneities (e.g., Tung & Masterlark, 2016). If the fault geometry is not reasonably well known, the uncertainty of the geometry may propagate into the fault slip determination (e.g., Ragon et al., 2018) and also bias the isolation of the effects of topographic relief and/or crustal heterogeneities. Broadly, the relative importance of unmodeled elastic structure or topographic relief and the uncertainty of fault geometry on surface deformation and fault slip inversion, and the importance of unmodeled elastic structure and topographic relief on fault geometry inversion have not been thoroughly documented, in part because of heavy computational demands of merging optimization approaches with the numerical tools needed to generate Green's functions (e.g., finite-element method [FEM] models; Tung & Masterlark, 2018; Tung et al., 2019).

The April 25, 2015 Mw 7.8 Gorkha, Nepal earthquake (and its largest aftershock) ruptured the downdip seismogenic zone (~10–20 km depth) of the Main Himalayan Thrust (MHT) at the plate boundary of India and Eurasian plates in Central Himalaya Arc (e.g., Avouac et al., 2015; Elliott et al., 2016; Hayes et al., 2015; Mencin et al., 2016; Figure 1). This event provides a good case example for assessing the impacts of topographic relief on determining the source location and geometry of a blind earthquake from geodetic observations given that the surface deformation field spans ~4.5 km of relief. In addition, seismological studies have revealed certain variations of seismic velocities in the vicinity of the 2015 Gorkha earthquake, implying the presence of crustal heterogeneities in both across-range and along-depth directions (e.g., Monsalve et al., 2006; Monsalve et al., 2008; Schulte-Pelkum et al., 2005). The topographic relief and crustal elastic structure have likely influenced the surface deformation field of the Gorkha earthquake such that an assumption of a homogeneous flat Earth may systematically bias inversions for fault geometry and slip. While we focus our examples on the Gorkha earthquake, our results are broadly applicable to understanding sources of modeling uncertainty in other similar thrust-style earthquakes.

In this study, we design three groups of forward and/or inverse FEM models to progressively investigate the impacts of topographic relief and crustal heterogeneity on coseismic deformation and earthquake source inversion. The main reason for using FEM models is their flexibility to account for the complex geometries and heterogeneity of the large-scale fault system. (1) We start with synthetic FEM forward models with an assumed slip distribution to illustrate the effects and the relative importance of topographic relief, crustal heterogeneity, and fault geometry (i.e., the dip angle, strike angle, and depth of the fault plane) on the model-predicted surface deformation of the Gorkha earthquake. (2) We next use homoge-

LI AND BARNHART 2 of 25

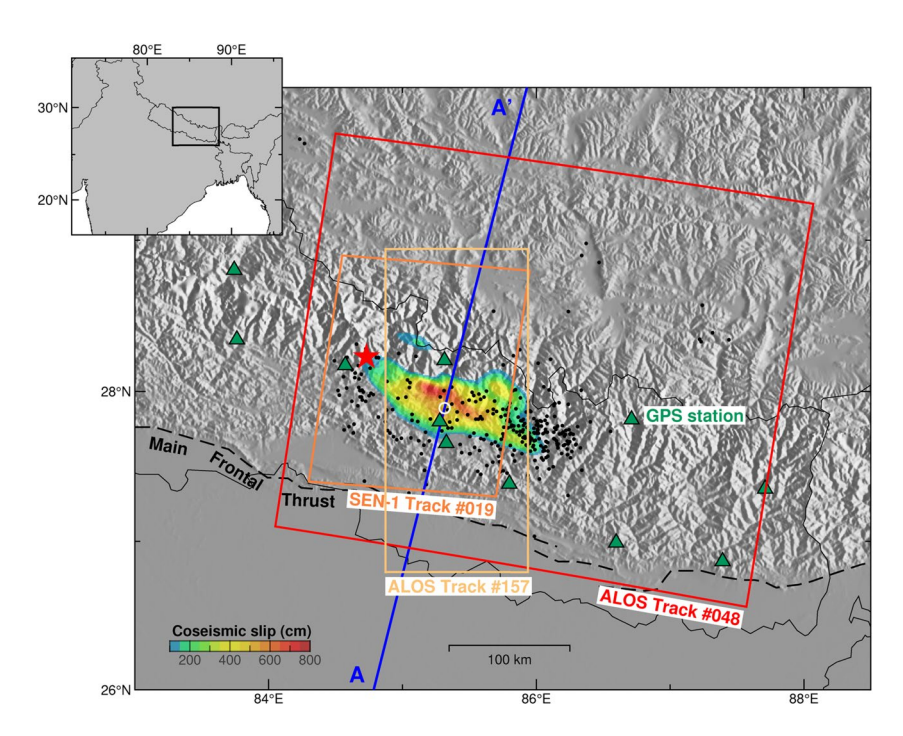


Figure 1. Tectonic settings of the study area. The red star and black dots denote the epicenter of the main shock and the aftershocks (>Mw 4) within 1 year (April 25, 2015 to April 25, 2016) after the 2015 Gorkha earthquake from National Earthquake Information Center (NEIC), US Geological Survey (earthquakes.usgs.gov). The coseismic slip distribution is from Elliott et al. (2016). The GPS locations are from McNamara et al. (2017). The white cycle is the map view of the reference point of the fault geometry. The blue line shows the location of profile in Figure 3. The gray shaded relief map is generated from the elevation model ETOPO1 (V9.1, Smith & Sandwell, 1997). GPS, Global Positioning System.

neous half-space models to invert the FEM-simulated synthetic surface displacement fields for the fault geometry and explore the bias of ignoring topographic relief and crustal heterogeneity on the recovery of true fault dip and depth. (3) Finally, we perform fault slip inversions of different fault geometries with and without topographic relief and crustal heterogeneity, based on FEM-generated Green's Functions and the real InSAR observations of the 2015 Gorkha earthquake. By quantitatively comparing the misfit of the inversions, we gain insights into the effects of the topographic relief and crustal heterogeneity on fault geometry and slip inversions with real geodetic data. We also explore the influences of inverted slip distribution due to the topographic relief and crust heterogeneity and the systematic variation of fault geometry.

2. InSAR Constraints

Since InSAR observations are much more spatially dense than the GPS observations (e.g., only five GPS offsets are available near the source area of the Gorkha event (McNamara et al., 2017, Figure 1), the model resolution of any geodetic inversions is dominated by the available InSAR constraints. For a representative case study, we therefore illustrate our forward model-predicted surface deformation in the line of sight (LOS) of InSAR observations and only use InSAR observations to constrain our FEM-based fault slip inversions. We assemble an InSAR data set of the mainshock of Gorkha event derived from the ALOS-2 and Sentinel-1 missions including two descending and one ascending tracks, published by Lindsey et al. (2015), Hayes et al. (2015), and McNamara et al. (2017) (Table 1; Figure 2). Together, this data set contains three independent looking angles of LOS displacements, potentially providing robust constraints on earthquake source inversions. We use the downsampled coseismic interferograms (in total 1,565 data points, Table 1) with a resolution of 5 km at best, and 8 km for most part of the deformed area (Figure S1), and their noise covariance structure (Lohman & Simons, 2005) in our FEM modeling.

LI AND BARNHART 3 of 25

Table 1 Parameters of Used Interferograms Pairs							
Satellite	Track #	Direction asc/dsc	Primary yyyy-mm-dd	Secondary yyyy-mm-dd	Downsampled data points	Averaged LOS vector ^a	
Sentinel-1	019	dsc	2015-04-05	2015-04-29	378	(-0.55; 0.11; -0.83)	
ALOS-2	048	dsc	2015-02-22	2015-05-03	745	(-0.62; 0.11; -0.77)	
ALOS-2	157	asc	2015-02-21	2015-05-02	442	(0.58; 0.11; -0.80)	
Abbreviation: LOS, line of sight.							

3. Forward and Inverse Modeling

3.1. FEM Model Setups

In this study, we conduct all FEM computations using the open-source finite element software PyLith (Aagaard et al., 2013), the accuracy and performance of which have been extensively tested in the benchmarks for the problems of dynamic earthquake rupture (e.g., Harris et al., 2018) and quasistatic crustal deformation (https://geodynamics.org/cig/working-groups/short-term-crustal-dynamics/benchmarks/). To minimize boundary effects, the lateral and depth dimensions of our FEM models are set significantly larger than the possible source dimension of Gorkha earthquake: 2,000 km long (east-west direction), 1,700 km wide (north-south direction), and 400 km high (vertical direction) (Figure S2a). In our models, all the lateral boundaries are fixed to have zero displacement in the normal direction but unconstrained in tangential directions. The basal boundary is fixed in the vertical direction but free in the horizontal directions. The top boundary is free in both horizontal and vertical directions. Our models consist of two domains (the hanging wall and foot wall) separated by the domain-separating fault plane. We use controlled meshing to gradually change the size of the tetrahedral elements in the areas of interest with finer element discretization size on the fault interface and top surface (about 8 km) and coarser element discretization size in foot wall (about 30 km) (Figure S2) with the software Cubit/Trelis (https://cubit.sandia.gov/). We use three parameters (dip, strike, and depth) to precisely define the spatial position of the fault plane (MHT) within the 3-D model space. For convenience of comparing fault geometries, the depth of the fault plane is defined as the distance of a reference point on the fault plane (latitude 85.4°, longitude 27.8°; Figure 3) to sea level (zero elevation). This point is chosen because large surface displacement is observed on the surface above it (~2,000 m elevation) and hence it is located within the main coseismic slip patch mapped by most previous studies (e.g., Elliott et al., 2016; Hayes et al., 2015; Lindsey et al., 2015; McNamara et al., 2017).

For any given fault geometry, we construct four FEM models to isolate the corresponding effects of topography and crustal heterogeneity: (1) a model with flat Earth surface (i.e., zero elevation is set on the top surface

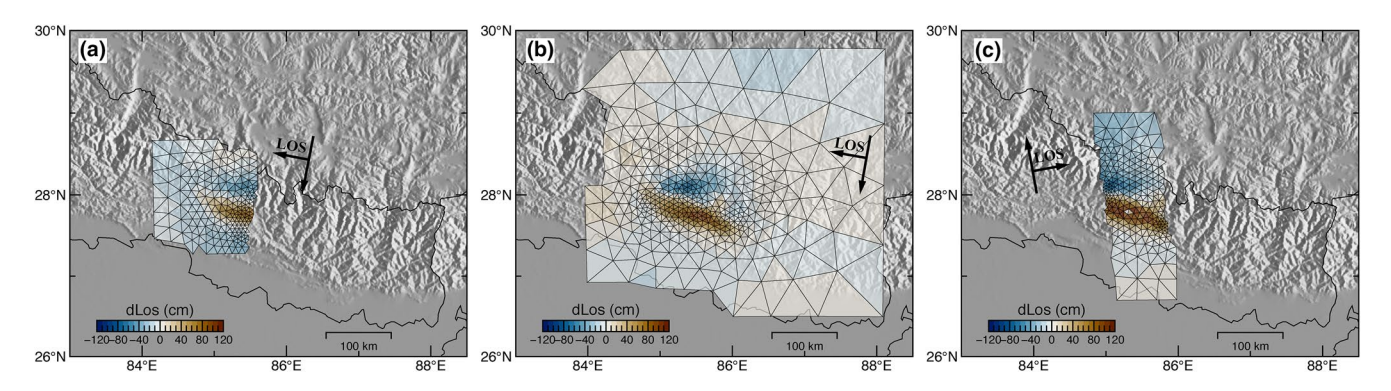


Figure 2. Used downsampled InSAR data of (a) Track #019, (b) #048, and (c) #157. The black arrows show the satellite azimuth and line of sight (LOS) directions. Positive and negative LOS values mean the surface toward and away from the satellite, respectively. Note that the data frames do not necessarily align with the satellite azimuth directions.

LI AND BARNHART 4 of 25

^aIn the coordinates system of East, North, and Up.

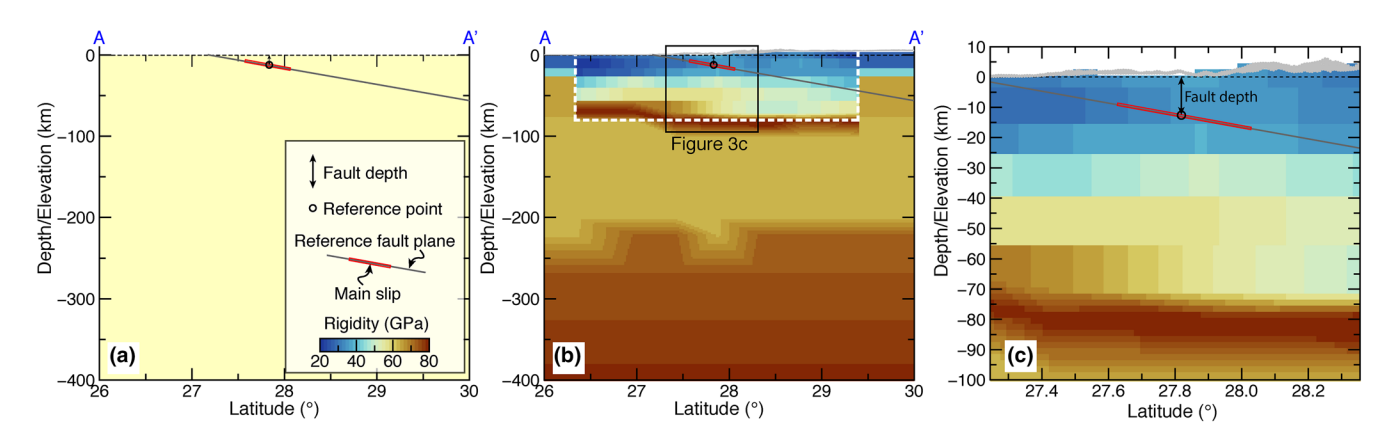


Figure 3. Topography and rigidity structure of two end-member models with the reference fault geometry. (a) The model with homogeneous elastic structure and flat Earth surface. (b) The model with heterogeneous elastic structure and realistic topographic relief. The gray dots are the elevations of the finite-element method top-surface points within a 10-km wide swath profile (see its location in Figure 1). The elastic properties within the white dashed lines are from the tomographic models of Monsalve et al. (2006, 2008) and those outside of the dashed lines are from the Preliminary Reference Earth Model. (c) A zoom-in plot of the model with heterogeneous elastic structure and realistic topographic relief.

of the model) and homogeneous material properties (Figure 3a), (2) a model with flat Earth surface and heterogeneous material properties, (3) a model with topographic relief and homogeneous material properties, and (4) a model with topographic relief and heterogeneous material properties (Figures 3b and 3c and Figure S3). Hereafter we name the four models as the "four end-member models" for convenience. The topographic relief is constructed using the elevation data from the updated ETOPO1 (V9.1) model, which has a spatial resolution of ~1.6 km in main rupture area of the Gorkha earthquake (Smith & Sandwell, 1997); the homogeneous material is characterized with a Young's modulus of 120 GPa, shear modulus (i.e., rigidity) of 48 GPa and Poisson's ratio of 0.25; the heterogeneous models incorporate the 2-D velocity structure from Monsalve et al. (2006, 2008) in the source region of the Gorkha earthquake, which have horizontal and vertical resolutions respectively of 70 km and 10-15 km, and material parameters outside of the source region of the Gorkha earthquake from the Preliminary Reference Earth Model (the rigidity structure in Figure 3b and the Poisson's ratio structure in Figure S3). Given possibly limited variations of the velocity structure in the strike (nearly east-west) direction of the study region, heterogeneous elastic properties in this study is defined mainly varying in the trench-normal (nearly north-south) and vertical directions (Figures 3b and 3c and Figure S3), consistent with previous studies of the Gorkha earthquake (e.g., K. Wang & Fialko, 2018). This elastic structure features relatively moderate gradients near fault and close to the ground surface (Figure 3b and Figure S3) and hence is expected to introduce limited impacts on coseismic surface deformation and inverted fault slip (Hsu et al., 2011; Williams & Wallace, 2018).

3.2. Forward FEM Simulations of Coseismic Surface Deformation

We first perform a series of FEM forward simulations to illustrate how the model-predicted coseismic surface deformation is affected by topography, crustal elastic structure, and fault geometry with an assumed coseismic slip distribution. We use the four end-member models with our reference fault geometry (dip 10°, strike 285°, and depth 12 km) to first illustrate the impacts of topography and crustal elastic structure. We denote the simplest model—that with no topography, homogeneous elastic structure, and the reference fault geometry—as the "REF Model." We project the slip distribution of Elliott et al. (2016) onto the fault plane in vertical direction (Figure S4) in our REF Model (in this way, the depth of the main slip does not vary significantly due to the change of the fault dip angle, Figure S4a) and the other three end-member models, and we perform the forward simulations. The kinematic fault slip is implemented in *PyLith* using the technique of "cohesive cells" for creating a fault interface, that is, the finite element mesh is replaced each fault face with a zero-volume cohesive cell in a preprocessing step at the beginning of a simulation (Aagaard et al., 2013). In this way, opposite motions of the two sides of the fault interface is achieved. We then calculate the synthetic InSAR observations of the three averaged satellite looking angles (Table 1) based on

LI AND BARNHART 5 of 25



the FEM-predicted 3-D surface deformation. We finally compare the synthetic LOS values from the four end-member models in map view and by histograms.

We then perform another 12 forward simulations to illustrate the impacts of the three parameters of the fault plane (dip, strike, and depth) and hence the potential uncertainty of fault geometry on the coseismic surface deformation. To isolate the impacts of each parameter, we fix two parameters of the fault geometry of the REF Model and vary the third one. In this way, we illustrate the contribution and relative importance of each parameter on surface deformation. We choose dip of 15°, strike of 290°, and depth of 9 km in comparison to the corresponding values of the reference fault geometry. For each parameter, we again construct four end-member models and investigate the potential coupling effects of fault geometry with topography or crustal elastic structure on surface deformation.

3.3. Inversions for Fault Dip and Depth With Homogeneous Half-Space and Synthetic FEM-Generated Surface Deformation

Fault dip and depth are utmost important geometric parameters on surface deformation according our forward simulations described in Section 3.2 (results are shown in Section 4.1). We therefore next focus on exploring the biases that might be introduced into the most commonly used half-space inversions for fault dip and depth, if topography and/or crustal elastic structure are ignored through a set of synthetic tests. We examine these biases by generating displacement fields that variously included and excluded the effects of topography and layered elastic structure with FEM models, and then inverting them for a faulting source using a homogeneous elastic half-space approximation (Okada, 1985). We simulate surface deformation originating from unit thrust slip on a buried fault plane with our FEM models. We test three different fault dips of 10°, 15°, and 30°. The strike and depth of the three fault models are fixed as 285° and 15 km. Similar to the forward simulations in Section 3.2, for each fault geometry, we generate the four sets of displacement fields from the four end-member models and consider the flat Earth model with homogeneous elastic structure as our experimental control. For LOS inversions, we generate synthetic coseismic interferograms by projecting each surface displacement field into ascending and descending LOS.

After deriving synthetic surface displacement fields, we generate 100 realizations of spatially correlated noise, each with the same covariance structure, for each look direction and add the synthetic noise to the noise-free displacement fields. Adding synthetic noise allows us to characterize how the inversions for fault geometry vary in the context of realistic noise. We then invert each synthetically noisy pair of ascending and descending interferograms for the best-fitting geometry (i.e., fault depth and dip) for a single slipping fault patch embedded in a uniform elastic half-space using the Neighborhood Algorithm (Okada, 1985; Sambridge, 1999). The median and 16th/84th percentiles are extracted as the preferred value and 1-sigma uncertainties given the non-Gaussian nature of the synthetic noise. Lastly, we conduct the same suite of inversions as described above using synthetically noise horizontal displacements fields in an effort to characterize how inversion of LOS displacements alone may bias inversions for faulting sources.

3.4. Inversions for Fault Slip With FEM Models and InSAR Observations

We finally conduct FEM-based inversions to investigate the influences of topography, crustal elastic structure, and fault geometry on fitting the real InSAR observations and determining the optimal fault slip distribution. We use FEM-generated Green's Functions (e.g., Li et al., 2015; Masterlark, 2003) and a bilinear orbit ramp function (e.g., Wright et al., 2004) to invert the real InSAR observations of the 2015 Gorkha earthquake (Figure 2) simultaneously for the fault slip distribution and the ramp signal of the InSAR data. FEM models are used to establish the linear system relating surface earthquake deformation to fault slip along the fault interface: $G \times s = d$, where \mathbf{s} is the parameter vector containing fault slip in both dip and strike directions (i.e., free rake), \mathbf{d} is the data vector (i.e., LOS displacements shown in Figure 2, and G is the matrix of Green's Functions depending on the fault geometry, material properties, and the surface topography of the FEM models. We generate the G matrix in the forward simulations, that is, LOS displacements at all the observational points caused by unit slip of the two slipping components (i.e., dip and strike) of finite-element fault nodes (Figure S5). We build up 72 fault planes in total by linearly sampling the three

LI AND BARNHART 6 of 25

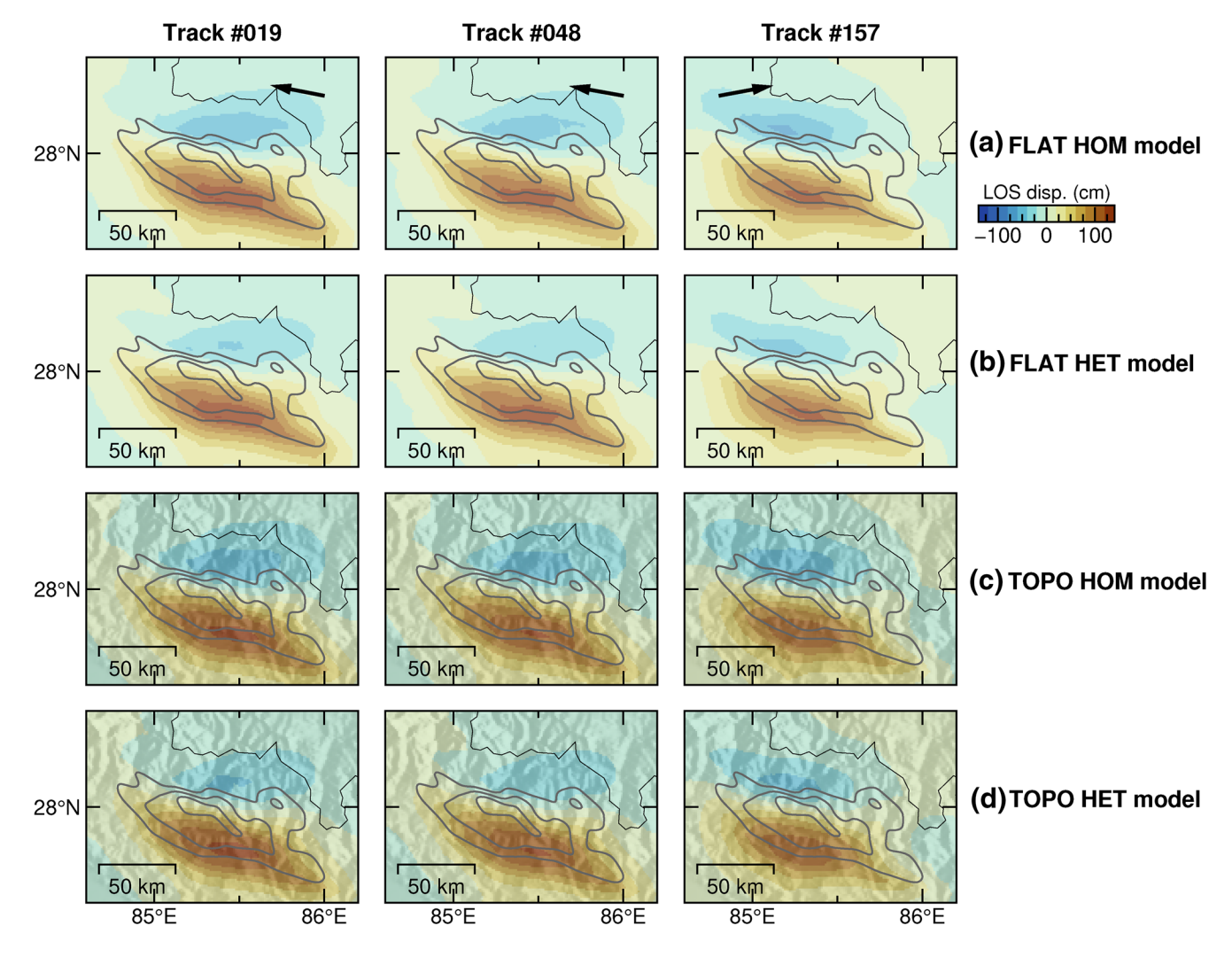


Figure 4. Surface deformation predicted from the four end-member models with the reference fault geometry (dip 10°, strike 285°, and depth 12 km). The black arrows in the Figure 4a indicate the line of sight (LOS) directions. The gray contours are the coseismic slip distribution from Elliott et al. (2016) in every 2 m. HOM, HET, and TOPO mean homogeneous, heterogeneous, and topography, respectively.

fault parameters (i.e., dips of 5°, 10°, 15°, 20°, 25°, and 30°; strikes of 280°, 285°, and 290°; depths of 9, 12, 15, and 18 km). We believe that these parameter combinations are of the most physically reasonable scenarios for the Gorkha earthquake. By systematically varying the three parameters, we gain insights into the propagation of the uncertainty of the fault geometry in the inversion results. In this study, we use the fault nodes in between longitude $84^{\circ}-87^{\circ}$ and at seismogenic depths (i.e., 0–30 km) to invert for fault slip. The number of fault nodes at this fault area decreases with the fault dip angle, resulting in \sim 4,000 fault nodes from the five dip angles (Figure S6). With three strike angles and four depths, we have in total \sim 47,000 fault nodes for all the fault geometries. With the four end-member models and two slipping manners for each fault geometry, we perform in total \sim 372,000 times of FEM forward simulations to assemble all the Green's Functions for fault slip inversions.

We evaluate the quality of slip inversions using the ${}_{j}R_{i}$ criterion (Barnhart & Lohman, 2010; Nealy et al., 2017). The ${}_{j}R_{i}$ misfit quantifies the degree to which a given slip distribution fits the true, underlying surface deformation signal while accounting for the spatially correlated nature of noise in the InSAR observations. Therefore, the lower ${}_{j}R_{i}$ misfit value also indicates the better InSAR data recovery of the inversion. For each FEM-based inversion, we present an optimal solution obtained with the minimum ${}_{j}R_{i}$ misfit. We then compare these minimum values of all the performed models and infer the optimal fault geometries

LI AND BARNHART 7 of 25

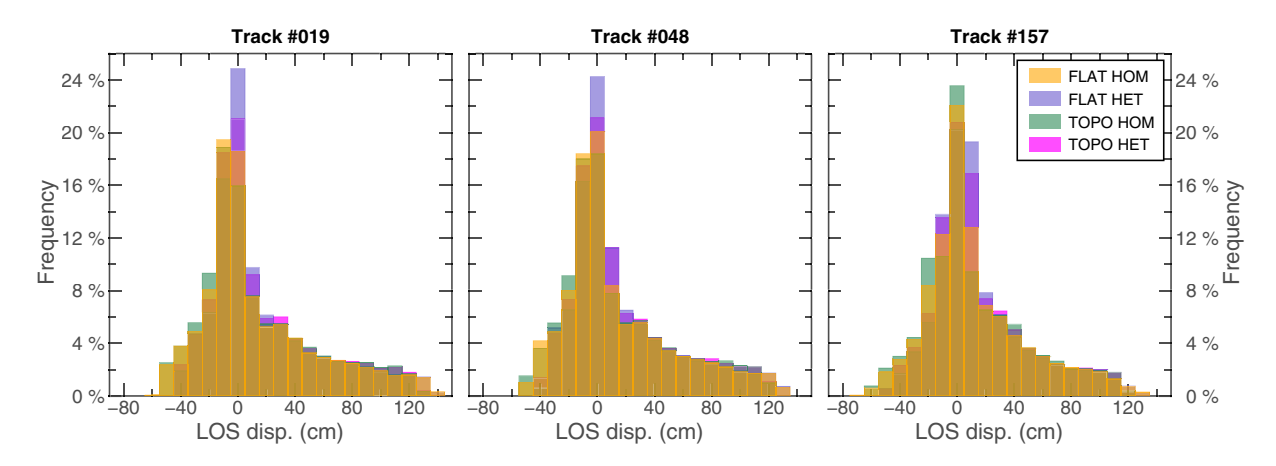


Figure 5. Histograms summarizing the predicted surface displacements from the four end-member models with the reference fault geometry (dip 10°, strike 285°, and depth 12 km) shown in Figure 4. HET, heterogeneous; HOM, homogeneous; LOS, line of sight; TOPO, topography.

for the four end-member models based on the lowest value of the minimum $_{j}R_{i}$ misfit. We also calculate the averaged slip along the fault strike direction as a function of fault depth to quantitatively compare the slip distributions from different inversions.

4. Results

4.1. Forward Modeling Results

The results of our forward simulations for the Gorkha earthquake are shown in Figures 4–11. The impacts of topography and crustal elastic structure on model-predicted coseismic surface deformation are summarized in Figures 4–7 and the impacts of fault geometry are summarized in Figures 8–11. Our results highlight that fault depth and dip angle have a relatively greater impact on coseismic surface deformation than fault strike angle, topography, and crustal elastic structure for the Gorkha case.

With the reference fault geometry, the predicted surface deformation from the four end-member models with the assumed slip distribution (maximum ~8 m) show clearly similar spatial patterns toward the satellite above the main ruptured area and away from the satellite in the north edge of the main rupture area (Figure 4), which are consistent with the InSAR observations (Figure 2) to the first order. Histograms of the predicted surface displacements (-60-120 cm LOS displacements) show that the four end-member models have similar skewed distribution of LOS magnitude frequency (i.e., statistically more positive displacements, Figure 5). Nevertheless, topography and crustal heterogeneity impact the magnitude of surface deformation (-10-10 cm LOS displacement), contributing maximally $\sim 10\%$ of displacement magnitude (Figure 7). For the specific seismotectonic settings of the Gorkha earthquake, the model including heterogeneous crustal elastic structure predicts larger surface displacements in the north edge of the main rupture area and smaller displacements in the south of the main rupture area (Figure 6a), spatially anticorrelating with the total predicted displacements (Figure 4). In contrast, topography has a more heterogeneous and localized impact on surface displacement (Figure 6b) and in general is opposite sense of the impact of heterogeneous crustal elastic structure (Figure 6a). Notably, the combined impacts of topography and crustal heterogeneity are greater than when topography or crustal heterogeneity are considered by themselves (Figure 6c). Histograms of the surface displacements contributed by topography and crustal heterogeneity generally have distinct distributions in magnitude frequency (Figure 7).

By increasing fault dip angle 5°, the four end-member models consistently predict smaller surface displacements when applying the same distribution of slip in comparison to the four end-member models with the reference fault geometry (Figure 8). The histograms of displacement frequency (-25-10 cm LOS displacement) show similar skewed distributions of the four models (more negative displacements, Figure 11a). By increasing the fault strike angle by 5°, the four models predict no significant difference of surface

LI AND BARNHART 8 of 25

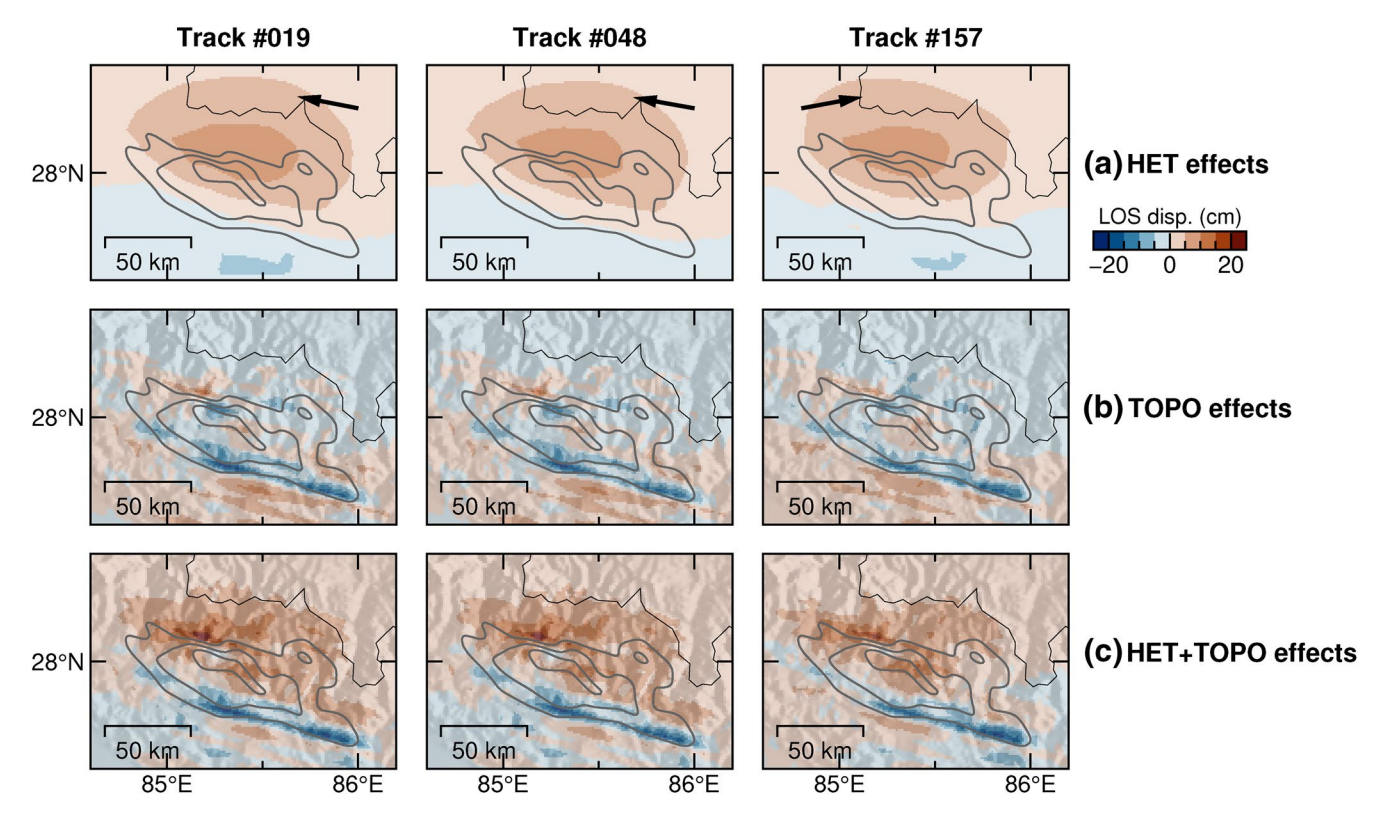


Figure 6. The impacts of topography and crustal heterogeneity on model-predicted surface deformation. Results in Figures 6a–6c are calculated by subtracting the LOS values of Figures 4b–4d with that of Figure 4a, respectively. The gray contours are the coseismic slip distribution from Elliott et al. (2016) in every 2 m. HET, heterogeneous; LOS, line of sight; TOPO, topography.

deformation in both space pattern (Figure 9) and displacement magnitude (-10-10 cm LOS displacement, Figure 11b). The corresponding topography and crustal heterogeneity effects (Figures S7 and S8) are insignificant in comparison to the effects of fault dip and strike (the differences of color-coded histograms in Figures 11a and 11b) for the Gorkha earthquake. By decreasing fault depth 3 km, the four models predict heterogeneous variation of surface displacement in map view (Figure 10). Interestingly, the surface deformation fields for the shallow source from the homogeneous and heterogeneous models are similar to each other (Figure 11c). But, the surface deformation fields of the flat and topography model are systematically

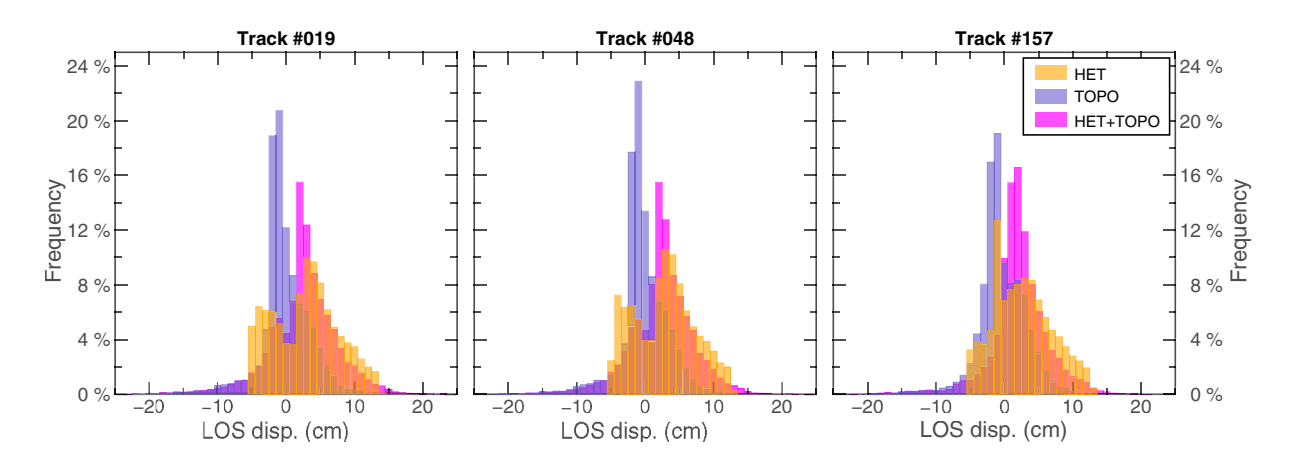


Figure 7. Histograms summarizing the impacts of topography and crustal heterogeneity on surface deformation shown in Figure 6. HET, heterogeneous; LOS, line of sight; TOPO, topography.

LI AND BARNHART 9 of 25

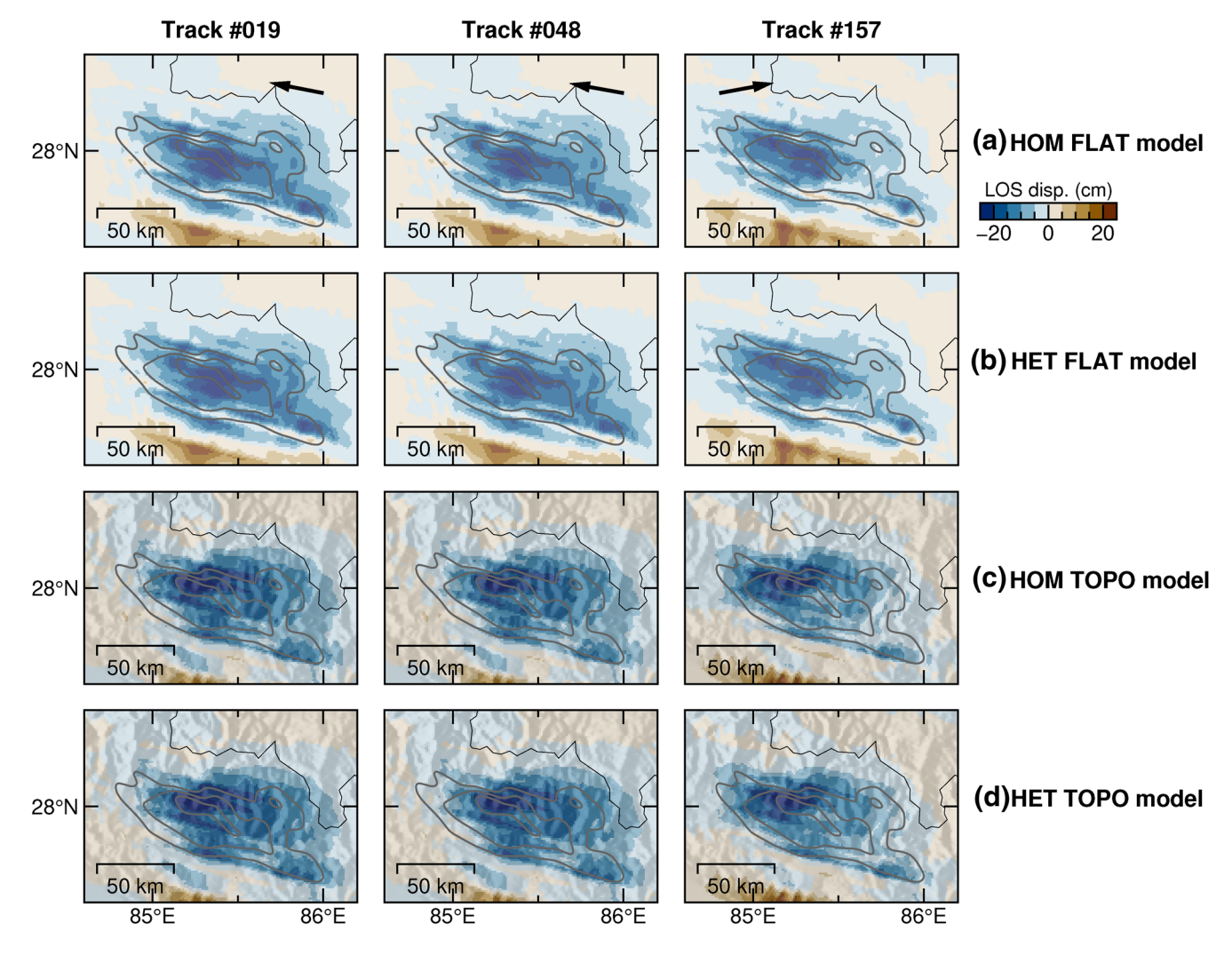


Figure 8. The impacts of fault dip angle on predicted surface deformation. The LOS displacements are calculated by subtracting the predictions of the comparing model (fault dip angle 15°) from those of the REF Model. HET, heterogeneous; HOM, homogeneous; LOS, line of sight; TOPO, topography.

different (Figure 11c). These changes of topography effects due to earthquake source depth change are also clear in spatial patterns (comparing Figure 6 and Figure S9).

We note that the forward modeling results presented in this section are based on the assumption of a certain coseismic slip distribution, which can also be influenced by topography, crustal heterogeneity, and fault geometry in slip inversions as we will show in the Section 4.3.

4.2. Half-Space Inversion Results

Summaries of the results of our half-space inversions of synthetic surface displacements for fault dip and fault depth are shown in Figures 12 and 13, respectively. Note, we here only provide a general discussion of trends and statistical behaviors of these inversions because specific uncertainties will vary from case to case and as a function of orientation of the fault plane with respect to LOS directions. Nevertheless, our results highlight that when inverting LOS displacements, including heterogeneous elastic structure tends to overestimate the fault dip and including topography tends to overestimate the fault depth. Moreover, the horizontal displacements fields place more robust constraints on both fault dip and depth than LOS observations.

LI AND BARNHART 10 of 25

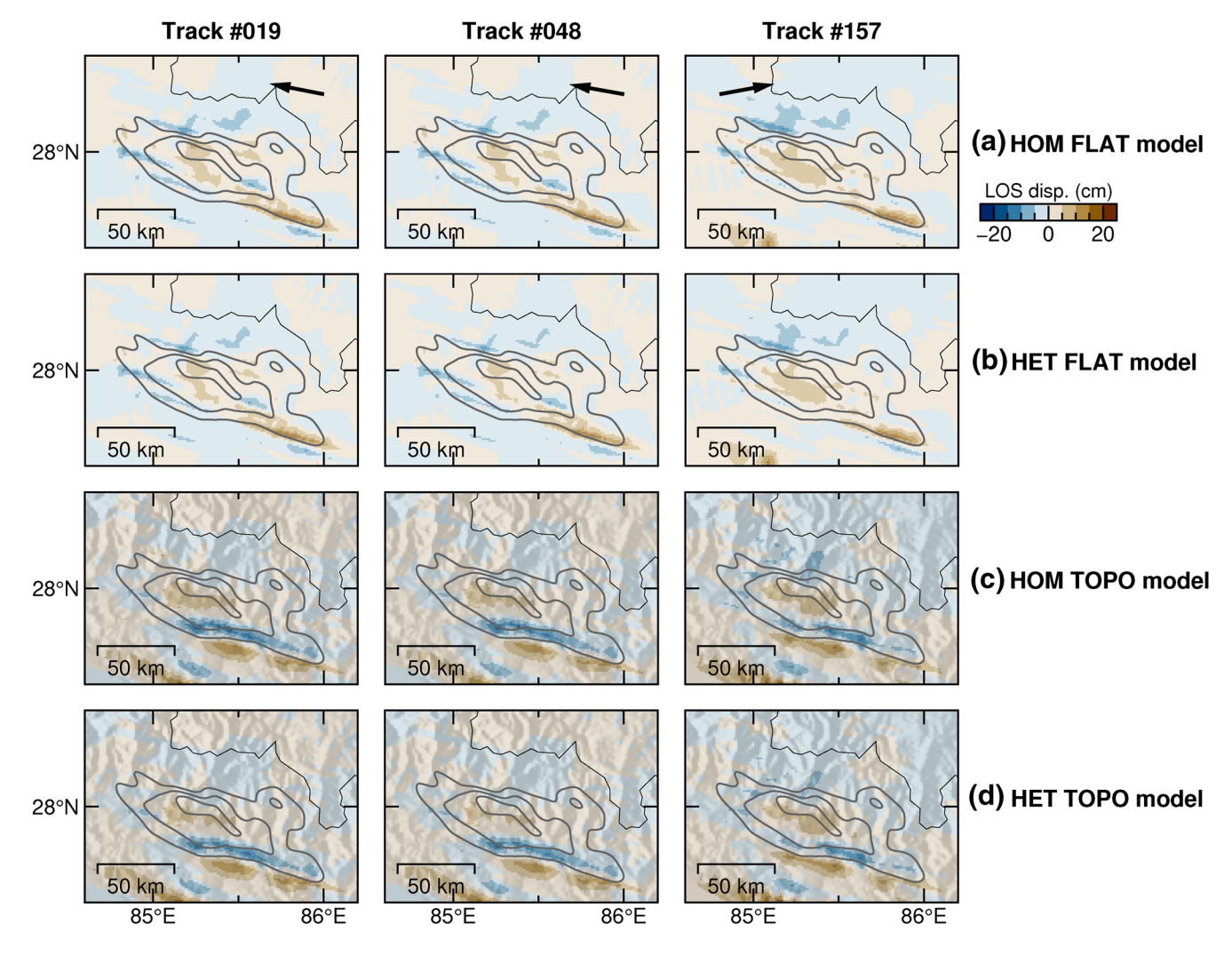


Figure 9. The impacts of fault strike angle on predicted surface deformation. The LOS displacements are calculated by subtracting the predictions of the comparing model (fault strike angle 290°) from those of the REF Model. HET, heterogeneous; HOM, homogeneous; LOS, line of sight; TOPO, topography.

In the context of recovering fault dip by inverting LOS displacements assuming a homogeneous, elastic half-space, we find that inversions routinely overestimate the dip angle (biased toward steeper dips) regardless of whether there are effects from topography and/or elastic heterogeneity in the displacement field. Within 1-sigma uncertainty, we are able to recover the true dip in cases where the true Earth structure is homogeneous, regardless of the effects of topography (Figures 12a–12c). The only exclusion to this trend occurs in the case of the 10° dip where we are not able to recover the true underlying dip of models produced in a homogeneous flat Earth FEM model to within 1-sigma uncertainty (i.e., the Okada-like input model is not recovered by Okada Green's functions) (Figure 12a). As we discuss further below, we believe this occurs because of LOS effects. In all three dip scenarios, inversions of displacements fields produced within a heterogeneous Earth structure are biased toward steeper dip values than those produced within a homogeneous Earth structure. As the true dip angle increases from 10° to 15° and finally to 30°, we find that the median value of our inversions with homogeneous Earth structure approach the true dip value. We observe no clear correlation between the presence of topographic effects and inferred dip angle (Figures 12a–12c).

Our tests that invert horizontal displacements rather than LOS displacements exhibit starkly different results (Figures 12d and 12e). First, the 1-sigma uncertainty ranges are comparatively narrower for each test, indicating the horizontal displacements fields place more robust constraints on fault dip than LOS observa-

LI AND BARNHART 11 of 25



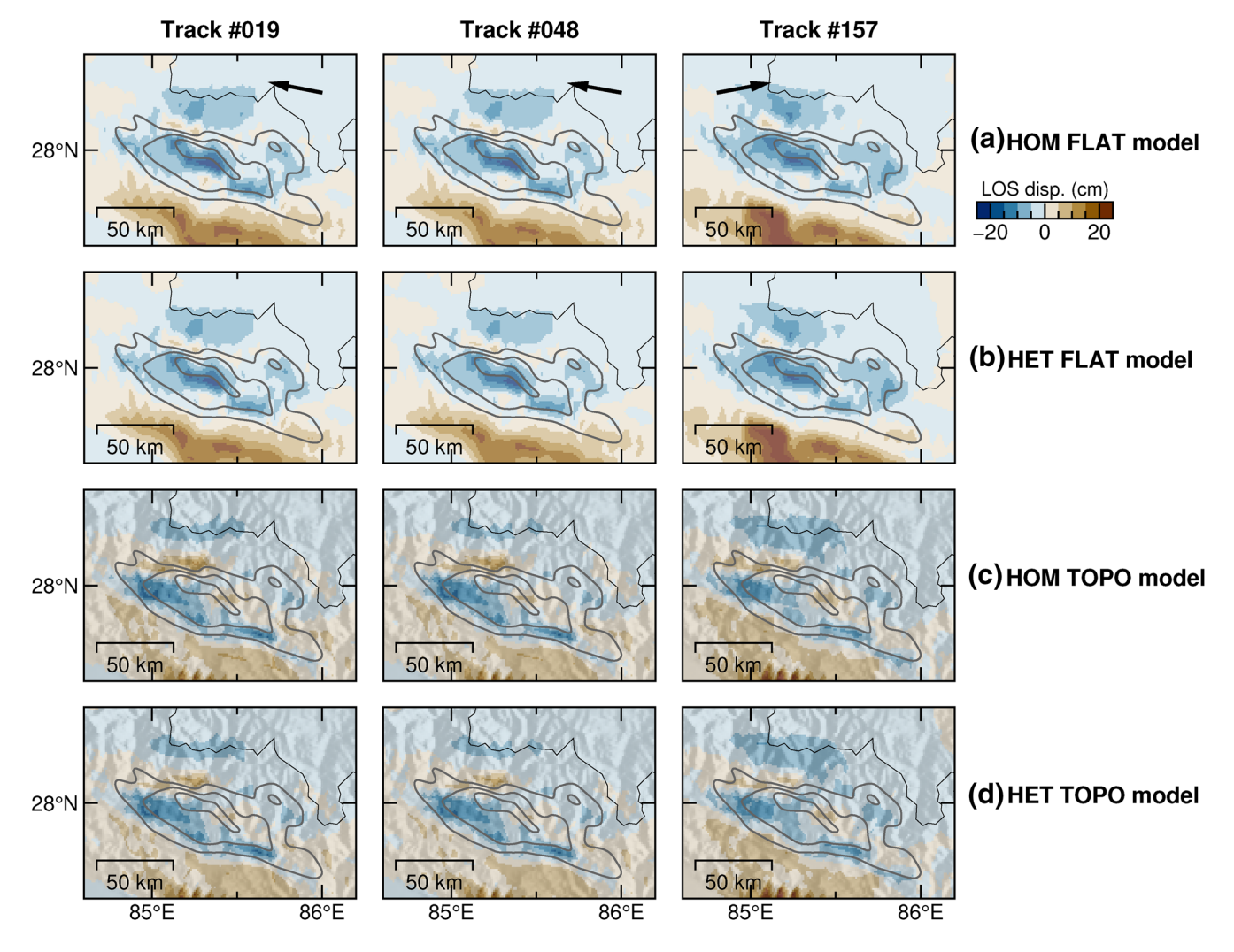


Figure 10. The impacts of fault depth on predicted surface deformation. The LOS displacements are calculated by subtracting the predictions of the comparing model (fault depth 9 km) from those of the REF Model. HET, heterogeneous; HOM, homogeneous; LOS, line of sight; TOPO, topography.

tions. As with the LOS inversions, we find that inversions of displacement fields with heterogeneous Earth structure effects group together; though, they tend to underestimate the true dip rather than overestimate it. We also find that we can recover the true dip value for displacements produced within a homogeneous flat Earth with a homogeneous flat Earth model for the dip ranges tested (Figures 12d and 12e). In all of our inversion tests (LOS and horizontal displacements fields), we find that uncertainty ranges systematically increase with increasing dip angle (Figure 12). These trends likely arise because as dip angle increases, the certainty on depth improves and a comparatively wider range of dip values can fit the observations. Conversely, at shallower angles, a narrower range of dip angle fit the data while depth is relatively unconstrained. These tradeoffs were demonstrated in the case of afterslip along a nearly flat decollement in the Zagros Mountains (Barnhart et al., 2018).

In the context of recovering fault depth from inversions of LOS displacements generated from different dip angles (Figures 13a–13c), we find that we are able to routinely recover the true depth in cases where the displacement field includes no topographic effects. Inversions of displacement fields with topographic effects are generally deeper than those without topographic effects; though, we do not see a consistent trend of this discrepancy increasing or decreasing with increasing dip angle (Figures 13a–13c). At the steepest tested dip (30°), all model groups recover the true depth to within uncertainty. We also observe that, with the exception of the 30° dipping scenario where all models converge toward the true depth, models with

LI AND BARNHART 12 of 25

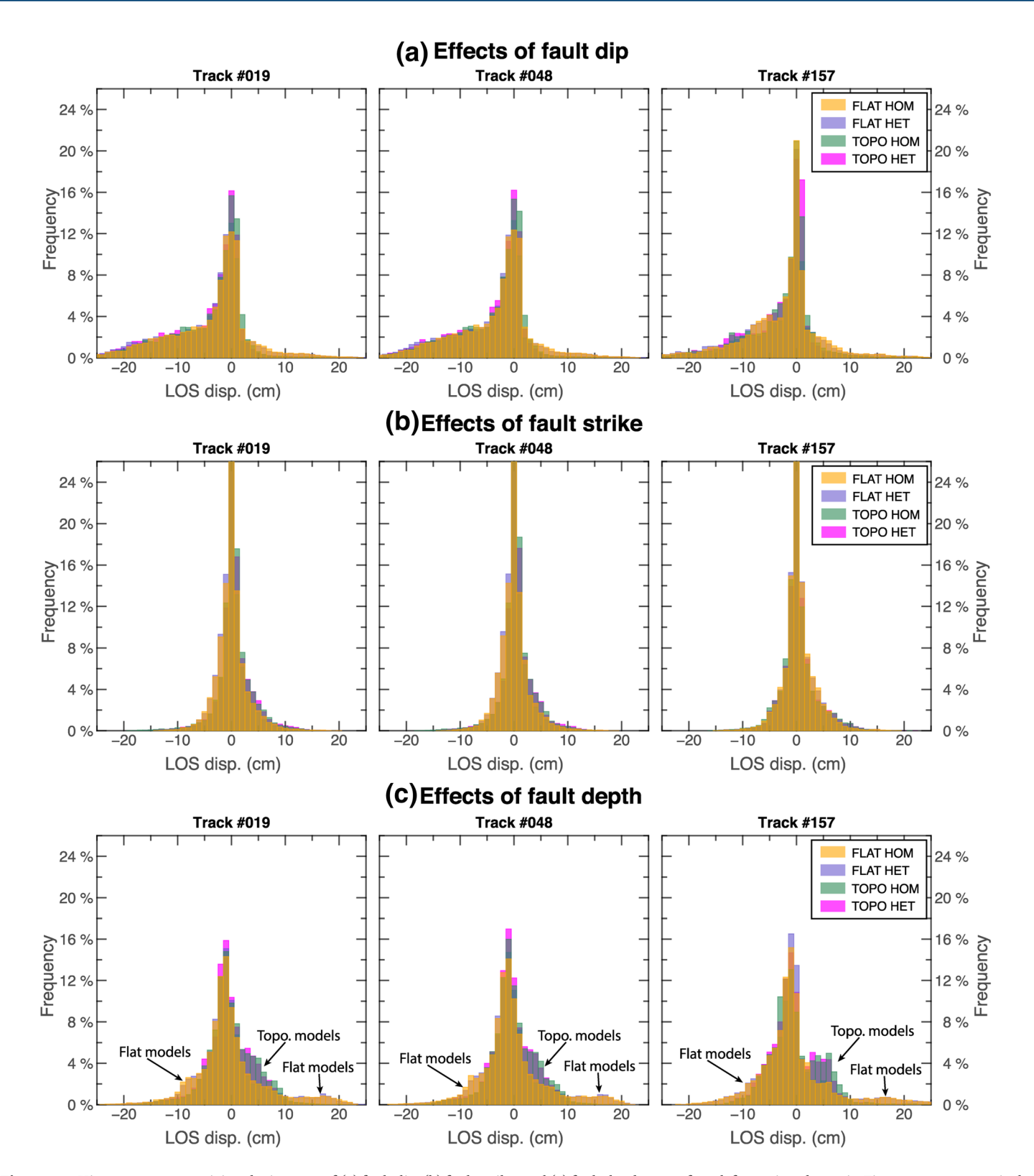


Figure 11. Histograms summarizing the impacts of (a) fault dip, (b) fault strike, and (c) fault depth on surface deformation shown in Figures 8–10, respectively. HET, heterogeneous; HOM, homogeneous; LOS, line of sight; TOPO, topography.

LI AND BARNHART 13 of 25

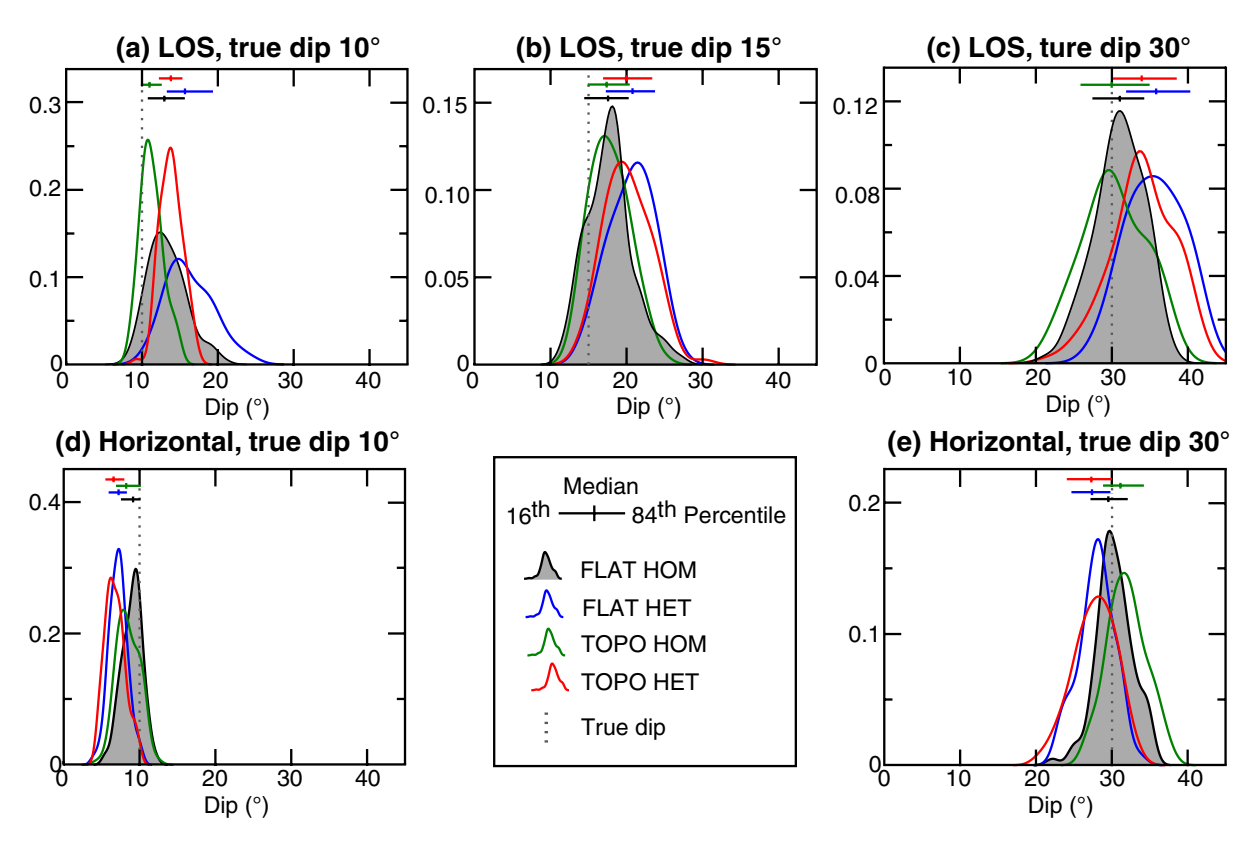


Figure 12. Probability density of fault dip recovery using homogeneous half-space models. (a–c) are determined by using synthetic InSAR displacements from FEM models. (d–e) are from using synthetic horizontal displacements from FEM models. FEM, finite-element method; HET, heterogeneous; HOM, homogeneous; InSAR, interferometric synthetic aperture radar; LOS, line of sight; TOPO, topography.

topographic effects group together in a similar way to how models without topographic effects group together (Figures 13a–13c).

Our inversions of horizontal displacements exhibit different depth distributions than the LOS inversions (Figures 13d and 13e). The inversions from horizontal displacements encompass systematically narrower uncertainty ranges, yet they tend to systematically underestimate the depth of the fault plane. In both the 10° and 30° dipping cases, we are not able to recover the true depth to within uncertainty in our control group inversions; whereas, we are able to recover the true depth to within uncertainty where the displacement fields have topographic effects. These relationships in part reflect the unique relative orientations between fault geometry, slip direction, and LOS of the Gorkha earthquake, but they additionally highlight important general considerations with respect to inverting LOS observations for fault depth.

4.3. FEM Inversion Results

The results of our FEM inversions are shown in Figures 14–18. Note, we are not aiming for determining a best slip distribution or a best faulting source because of the huge model parameter spaces and various inversion regularizations, but for illustrating the general influences of topography, crustal heterogeneity, and fault geometry on the slip distribution for the Gorkha earthquake. In this perspective, our results highlight that fault geometry parameters are more sensitive to geodetic inversions than topography and crustal heterogeneity in terms of recovering the geodetic data for the Gorkha case. Moreover, the fault dip angle and depth can systematically influence the inverted slip distributions in the presence of topographic relief and crustal heterogeneity.

Based on the minimum $_jR_i$ misfit values of all the inversions (Figure 14), the optimal fault geometry parameters are obtained respectively for the four end-member models (Table 2). The optimal fault depth (12 km)

LI AND BARNHART 14 of 25

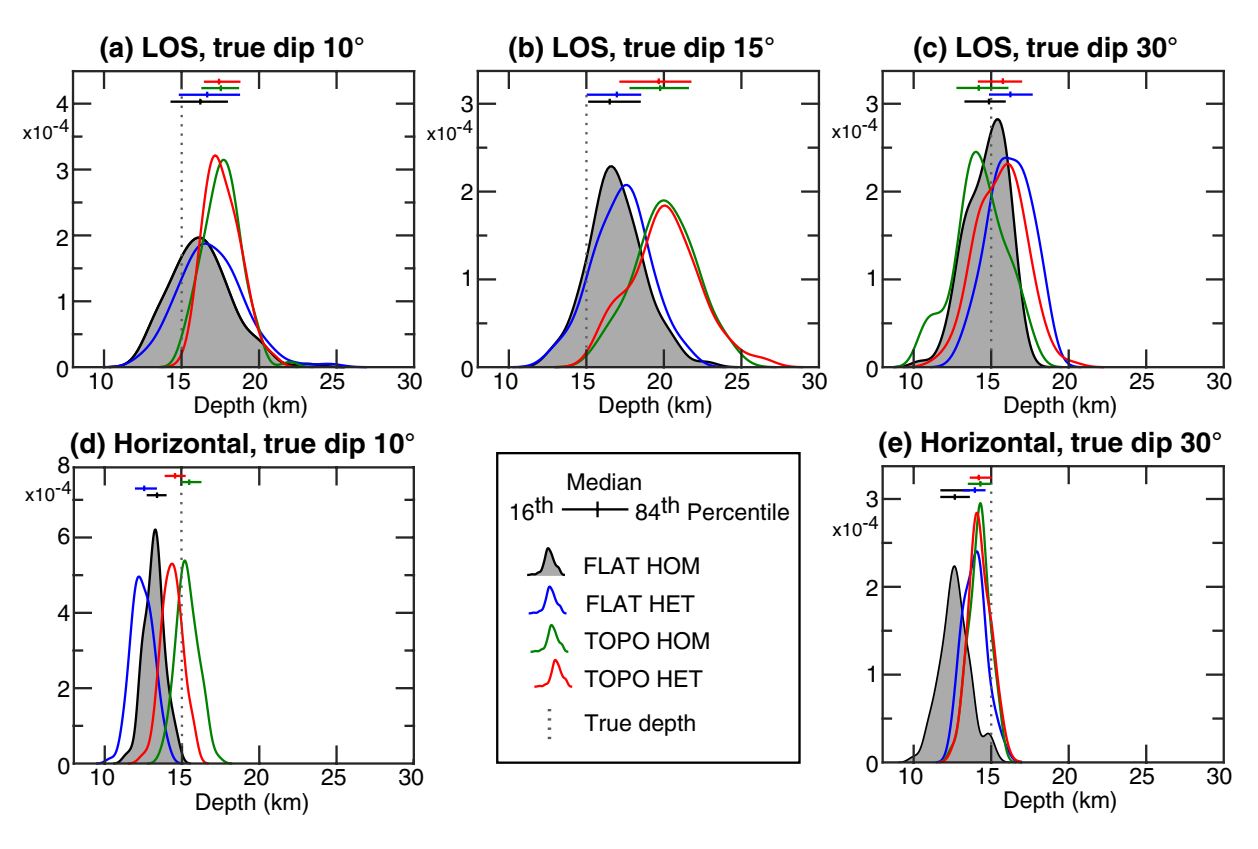


Figure 13. Probability density of fault depth recovery using homogeneous half-space models. (a–c) are determined by using synthetic InSAR displacements from FEM models. (d–e) are from using synthetic horizontal displacements from FEM models. FEM, finite-element method; HET, heterogeneous; HOM, homogeneous; InSAR, interferometric synthetic aperture radar; LOS, line of sight; TOPO, topography.

and dip angle (20°) are the same for all the four models. Although it is not distinct judging from the minimum $_jR_i$ misfit values (Figures 14a and 14b), the optimal fault strike angle (285°) for the models with topography is proposed to be relatively larger than that (280°) for the models with flat surface. Homogeneous and heterogeneous models show no significant difference in recovering the InSAR data, regardless of including topography or not in the FEM models (i.e., blue and red dots are largely overlapped in Figures 14a and 14b). Models with topography and flat surface show certain deviation from each other with the same geometric parameters (i.e., blue and red dots are not overlapped in Figures 14c and 14d) but they perform quite similarly in explaining the InSAR data and hence determining the optimal geometric parameters (i.e., minimum $_iR_i$ values of blue and red dots in Figures 14c and 14d).

Using the common optimal fault geometry of the four end-member models (i.e., dip 20° , strike 285° , and depth 12 km, Table 2) as a reference, we further show the influence of varying each of the three parameters on the optimally inverted fault slip distributions (i.e., the solutions obtained from the minimum $_{j}R_{i}$ values presented in Figure 14) by fixing the other two parameters (Figures 15–17). Larger fault dip angle leads to more concentrated slip distribution at depth (Figure 15), and the maximum and most slip of all the inversions are featured the same depth (10–15 km, Figure 15) or the same corresponding surface area (Figure 15); fault strike angle do not change significantly the slip distribution, but higher strike angle tends to relate to more concentrated slip distribution (Figure 16); deeper fault depth results in deeper slip distribution, larger maximum slip, and more shallow-skewed slip distribution (Figure 17). These influences of fault geometry on inverted slip distribution are not biased by the presence of topography and heterogeneous crustal elastic structure (comparing the four panels in Figures 15–17 and stacking the slip distributions of all the inversions in Figure 15). The impacts of topography and crustal heterogeneity, and the variations of fault geometry together lead a fruitful variety of the slip distributions but mainly a blind slip patch at depth (Figure 15).

LI AND BARNHART 15 of 25

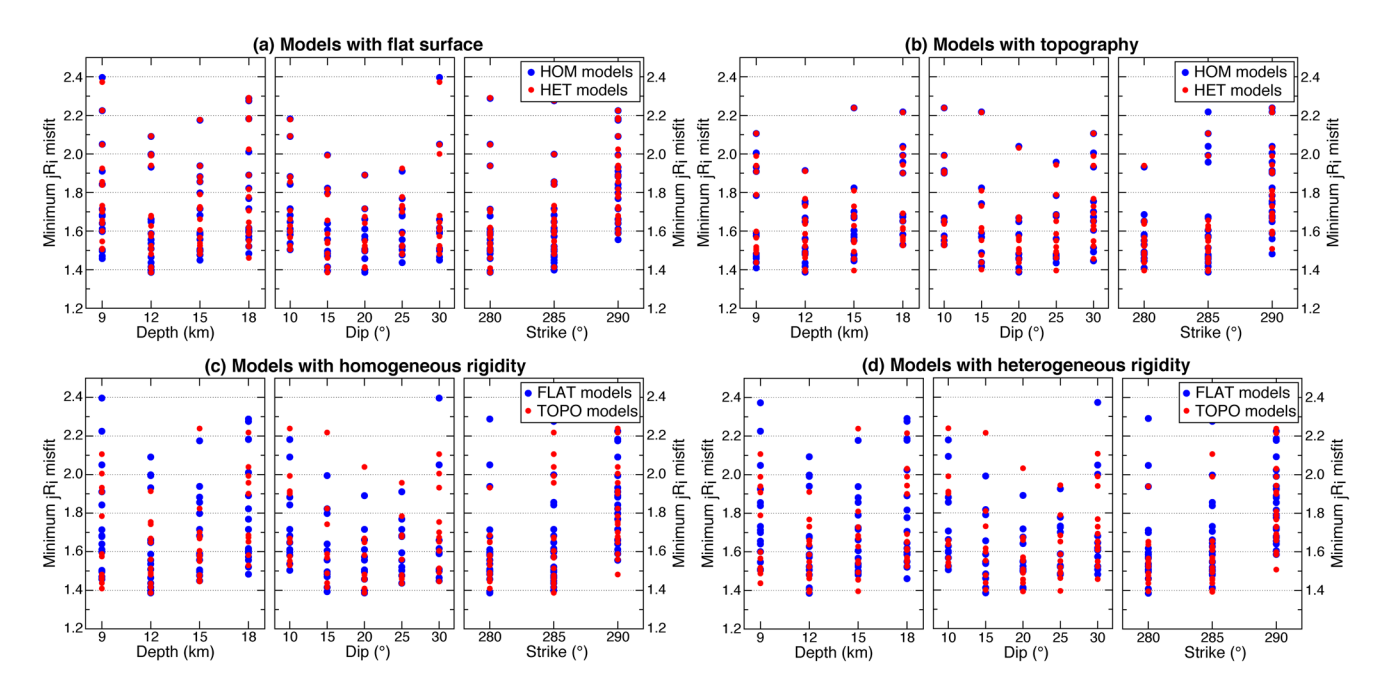


Figure 14. Minimum $_{j}R_{i}$ misfit as a function of the three parameters of the fault plane obtained from the fault slip inversions. All the performed models are plotted into four categories to highlight the impacts of topography and heterogeneous elastic structure: (a) and (b) show the comparisons of the models with homogeneous (blue dots) and heterogeneous (red dots) crustal elastic structure; (c) and (d) show the comparisons of the models with flat surface (blue dots) and topography (red dots). One color-coded dot represents the minimum $_{j}R_{i}$ misfit of one FEM-based slip inversion, which may be determined from different smoothing factors applied on the slip distribution for different models. FEM, finite-element method; HET, heterogeneous; HOM, homogeneous; LOS, line of sight; TOPO, topography.

The optimally inverted slip distributions from the optimal model with flat surface and homogeneous crustal elastic structure (Figure 18a) and the optimal model with topography and heterogeneous (Figure 18b) are similar to each other in terms of spatial pattern and maximum slip values. These two slip distributions are

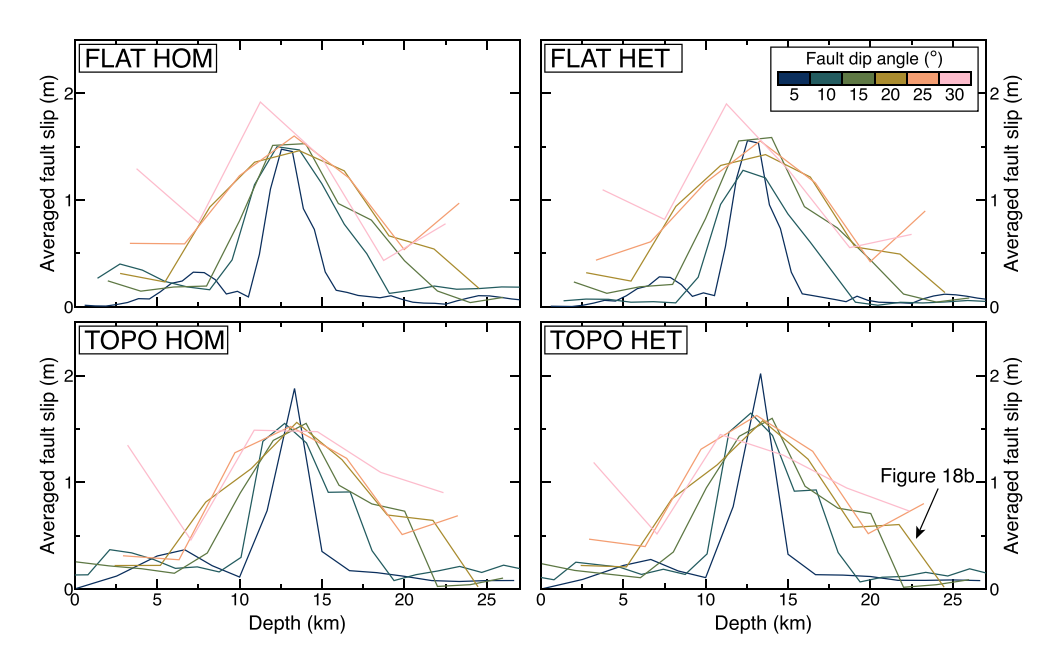


Figure 15. The impacts of fault dip angle on the optimally inverted slip distribution for the four end-member models. Fault strike angle and depth are fixed as 285° and 12 km, respectively. HET, heterogeneous; HOM, homogeneous; TOPO, topography.

LI AND BARNHART 16 of 25

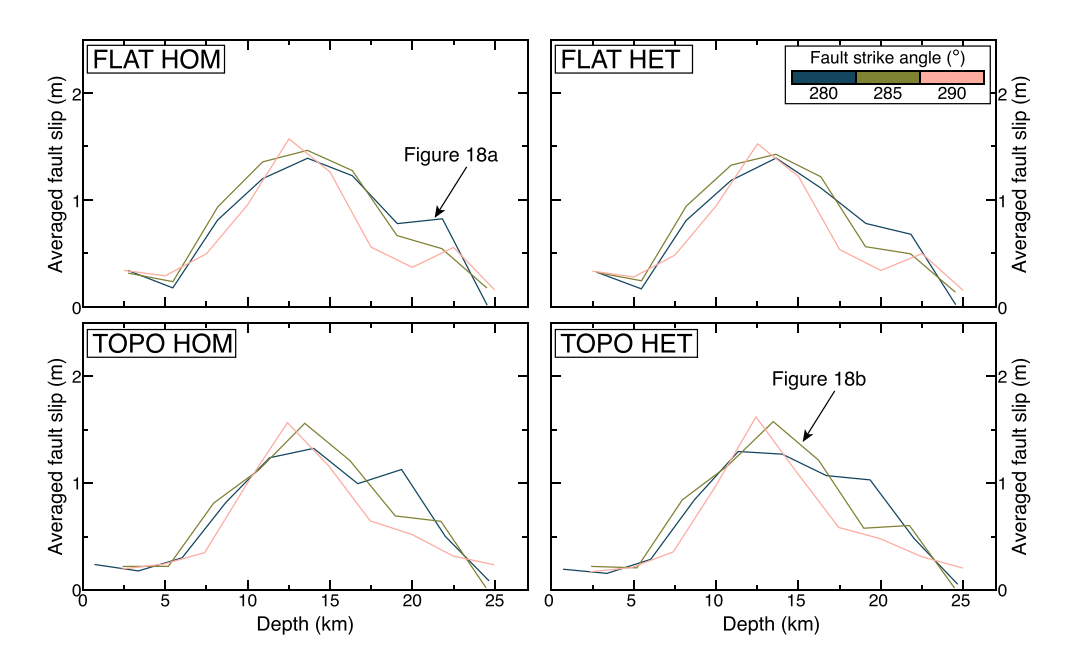


Figure 16. The impacts of fault strike angle on the optimally inverted slip distribution for the four end-member models. Fault dip angle and depth are fixed as 20° and 12 km, respectively. HET, heterogeneous; HOM, homogeneous; TOPO, topography.

largely consistent with previous studies but less slip in the deep part (north) of the fault, where the midcrustal ramp (i.e., larger fault dip angle) is suspected (e.g., Elliott et al., 2016). No significant difference of the two models is found in terms of explaining the InSAR observations (Figures 812 and 813).

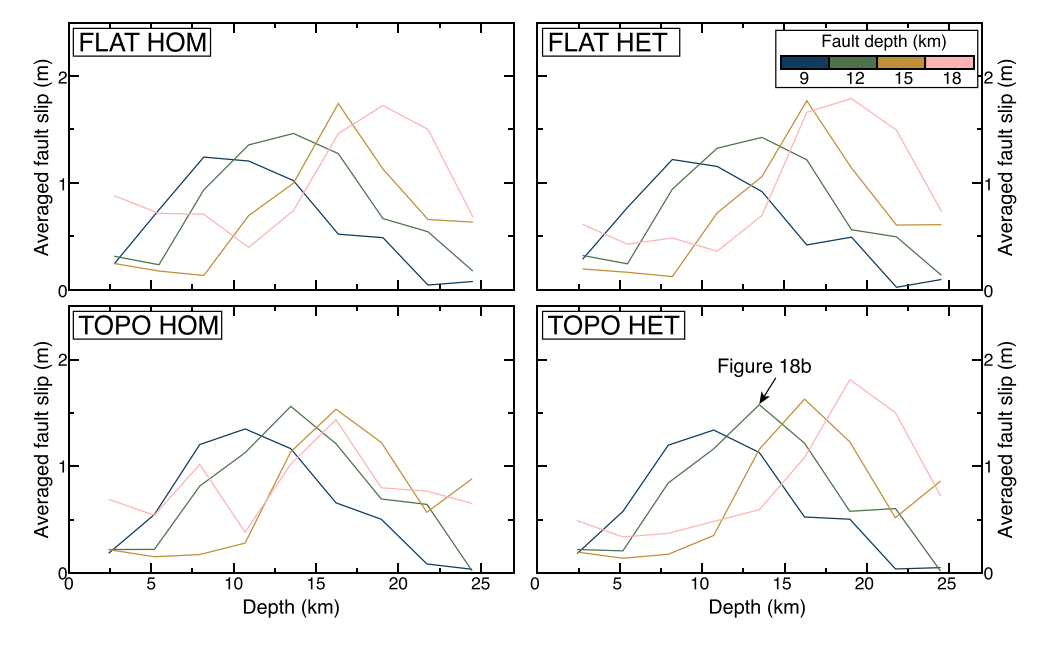


Figure 17. The impacts of fault depth on the optimally inverted slip distribution for the four end-member models. Fault strike and dip angle are fixed as 285° and 20°, respectively. HET, heterogeneous; HOM, homogeneous; TOPO, topography.

LI AND BARNHART 17 of 25

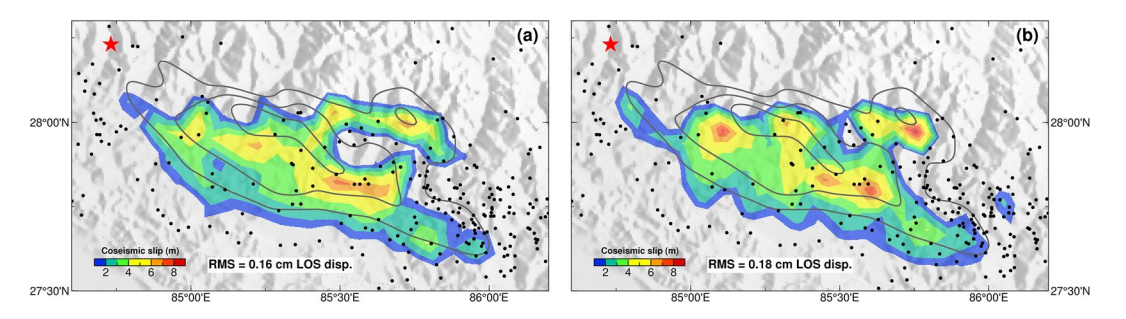


Figure 18. Optimally inverted coseismic slip distributions of (a) "FLAT HOM" model and (b) "TOPO HET" model with the corresponding optimal fault geometries. The fault geometry parameters of the "FLAT HOM" model are dip 20°, strike 280°, and depth 12 km. The fault geometry parameters of the "TOPO HET" model are dip 20°, strike 285°, and depth 12 km. The red star and black dots denote the epicenter of the main shock and the aftershocks (>Mw 4) within 1 year (April 25, 2015 to April 25, 2016) after the 2015 Gorkha earthquake from National Earthquake Information Center (NEIC), US Geological Survey (earthquakes.usgs.gov). The gray contours are the coseismic slip distribution from Elliott et al. (2016) in every 2 m. LOS, line of sight; RMS, root mean square.

5. Discussion

5.1. Impacts of Topographic Relief, Crustal Heterogeneity, and Fault Geometry on Coseismic Deformation

Our forward modeling experiments that impose the coseismic slip distribution of Elliott et al. (2016) suggest that excluding or including topography and/or crustal heterogeneity does not significantly change the pattern (Figure 4) and magnitude (Figure 5) of the expected surface deformation for the Gorkha earthquake. Exclusion/inclusion of topography and/or heterogeneous crustal elastic structure only contributes maximally ~10% of surface displacement magnitude (comparing Figures 5 and 7), consistent with previous studies for the Gorkha earthquake (e.g., K. Wang & Fialko, 2018). The reasons of such limited impacts of topographic relief and crustal heterogeneity for the Gorkha earthquake may be the relatively gentle topographic gradient above the ruptured zone of the Gorkha earthquake (Figure 3c) (Williams & Wadge, 2000) and the relatively moderate gradients of elastic structure (Figure 3b and Figure S3) used in our models (Hsu et al., 2011; Williams & Wallace, 2018), respectively. Earthquakes with higher or lower topographic and elastic-structure gradients may lead to more or less contributions on surface deformation from the topographic relief and crustal heterogeneity. Our forward models also confirm that topography and crustal heterogeneity impact the surface deformation in two different ways, consistent with previous studies (e.g., Langer et al., 2019), that is, crustal heterogeneity has more homogeneous effects in space and influences mainly the displacement magnitude (Figure 6a), and topography has more heterogeneous effects in space and influences mainly the deformation pattern (Figure 6b). These different impacts on the surface displacement magnitude may be able to be isolated by geodetic data in some cases, deserving further investigations (more discussion related to this in Section 5.5).

When varying the dip angle and depth of the fault plane, the corresponding four end-member models consistently show significant impacts of these fault geometry parameters on surface deformation (Figures 8

 Table 2

 Optimal Fault Geometry for the Four End-Member Models

L	<i>3 3</i>		
Model name	Depth (km)	Dip (°)	Strike (°)
FLAT HOM	12	20	280
FLAT HET	12	15/20	280
ТОРО НОМ	12	20	285
TOPO HET	12	20	285

 $\label{eq:homogeneous} Abbreviations: \ HET, \ heterogeneous; \ HOM, \ homogeneous; \ TOPO, topography.$

and 10) and the first-order similarity of the skewness of the histograms of displacement frequency (Figures 11a and 11c). These results suggest that these two fault parameters have a dominant control on surface deformation compared to the impacts of topography and crustal heterogeneity for this study. In contrast, the four end-member models show no significant variation of surface deformation when varying the fault strike angle (Figures 9 and 11b). This is not unsurprising given the relatively shallow dip (10°) of the fault plane we use to simulate the surface deformation. We additionally find some tradeoffs between the impacts of topography and crustal heterogeneity and the three parameters of fault geometry (i.e., different color-coded histograms do not fully overlap with each other in Figure 11). Most notably, the impacts of topography are clearly coupled

LI AND BARNHART 18 of 25



with fault depth (Figure 11c), indicating that the topography effects on surface deformation are not only correlated to the topography itself on surface but also sensitive to the depth of earthquake source (e.g., Williams & Wadge, 1998, 2000).

5.2. Recovery of Fault Dip and Depth With Homogeneous Half-Space Model

There are several important trends and relationships in the tests where we invert different displacement fields from FEM forward simulations with a homogeneous elastic half-space model. First, we are not able to recover the true underlying dip when we invert our 10° dipping LOS displacement control group (displacement field generated in a homogeneous flat Earth) with a homogeneous elastic half-space model (Figure 12a). Conversely, when we invert the same control group but with horizontal displacements, we are able to recover the true dip (Figure 12d). As dip angle increases to 15° and 30° dip (Figures 12b and 12c), we are able to recover the dip from the LOS displacement control group. This relationship occurs because our model is of thrust motion, and thrust motion on a shallowly dipping plane produces predominantly horizontal displacements that are not well resolved by LOS displacements. As dip angle increases, the relative magnitude of vertical displacements also increases and provides stronger constraint on the dip angle. This relationship was observed in uncertainties associated with inversions for the dip of nearly horizontal thrust planes associated with the Mw7.3 Darbandikhan (Sarpol-e-Zahab) earthquake in Iran in 2017 (Barnhart et al., 2018; Nissen et al., 2019).

Second, the distributions of inverted dip angle are divided into two groups: inversions of displacement fields with heterogeneous Earth structure effects and inversions of displacement fields with homogeneous Earth structure effects (Figure 12). These results indicate that inversions for fault dip are more sensitive to unmodeled elastic structure than they are to unmodeled topographic effects. Accordingly, one might reasonably assume that, for steep enough dips ($>\sim15^\circ$), the topographic effects can be ignored when attempting to resolve dip angle.

Third, our fault plane depth estimates show the opposite grouping as for dip. Here, the inversions are divided into two groups: inversions of displacement fields with topographic effects and those without topographic effects (Figures 13a–13c). Inversions of horizontal displacement fields do not exhibit as clear of a grouping (Figures 13d and 13e). We interpret this result to indicate that, when using LOS displacements, inversions for fault depth are more sensitive to unmodeled topographic effects than they are to unmodeled elastic structure.

5.3. Impacts of Topography, Crustal Heterogeneity, and Fault Geometry on Fault Slip Inversion

Although the synthetic forward modeling results clearly show the impacts of topography and crustal heterogeneity on surface deformation (Figures 6 and 7), our inversions for fault slip indicate that it is difficult to isolate the effects introduced by topography or crustal structure in terms of explaining the observed surface deformation for the Gorkha earthquake (Figure 14), consistent with some of the previous case studies (e.g., Hsu et al., 2011; Simons et al., 2002; K. Wang & Fialko, 2018). Nevertheless, in tests where we explore the impacts of topography show systematically different data misfit for many geometry parameter combinations (i.e., many red and blue dots do not overlap with each other in Figures 14c and 14d) mainly because the impact of topography on surface deformation is related to the earthquake depth (Figures 10 and 11c). Therefore, studies investigating the topography effects on coseismic deformation and fault slip distribution have to reasonably constrain the fault depth first. In contrast, our inversion that just explores the impacts of crustal elastic heterogeneity show similar data misfit for most geometry parameter combinations (i.e., red and blue dots overlap largely with each other in Figures 14a and 14b). Considering a large variability of possible fault geometries, our inversions show that the fault geometry parameters are more sensitive to the model misfit than the topography and crustal heterogeneity for the Gorkha earthquake (Figure 14). Therefore, geodetic earthquake source models have to incorporate the first order uncertainty of fault geometry (e.g., Ingleby et al., 2020; Ragon et al., 2018) before further considering the effects of topography and crustal heterogeneity.

LI AND BARNHART 19 of 25



Our FEM inversions additionally show some but no systematic impacts of topography, crustal heterogeneity, and fault strike angle on the inverted slip distributions (e.g., no significant difference of the results from the four end-member models in Figures 15–17). In contrast, the dip angle and depth of the fault plane can systematically trade off the determined slip distributions in the presence of topographic relief and crustal heterogeneities (Figures 15 and 17). With fixed fault strike angle and depth, larger fault dip angle results in more distributed slip distributions along depth (Figure 15) but does not change the depth (10–15 km) of the main slip (Figure 15) or its corresponding location on Earth's surface (Figure S10) where most surface deformation were observed. With fixed fault dip and strike angles, deeper fault depth leads to deeper-skewed and larger maximum slip value of the slip distributions (Figure 16). These results suggest that different assumptions of fault dip angle and depth will strongly bias the fault slip inversion, partly explaining the large variety of published slip distributions for a given earthquake. In addition to the explored influences of topography, crustal heterogeneity and fault geometry in this study, we should notice that the imposed inversion constraints (e.g., the smoothing factor applied to the slip distribution, Li, Wang et al., 2018) and data coverage (e.g., Williamson & Newman, 2018) can also influence the inverted slip distribution.

5.4. On the Ramp-Flat Structure

An important geometrical feature of MHT that hosted the 2015 Gorkha earthquake is the downdip portion of the MHT in a region encompassing along-dip geometric changes (i.e., fault dip angle $\sim 30^{\circ}$) in the middle crust, named "ramp-flat" structure (e.g., Hubbard et al., 2016). The presence of a ramp fault segment is thought to influence the interseismic strain accumulation (e.g., Pandey et al, 1995) and earthquake occurrence time (Li, Barnhart et al., 2018). Since a ramp-flat geometry essentially increases both fault dip angle and depth in the downdip portion of the fault in comparison to a flat fault without a ramp segment, our inversion results suggest that the ramp-flat structure requires more geodetically inverted slip on the ramp segment. This explains why the slip model of Elliott et al. (2016), which considered a ramp-flat fault geometry, obtains more slip in the northern deeper area of the main rupture zone than our planar fault models (Figure 18). Despite this difference, models with planar and ramp-flat fault geometries both feature most of the coseismic slip on the shallower area (Figure 18). Ignoring the ramp segment in our planar fault geometry, our inversions may overestimate some slip in the downdip portion of the fault and yield a larger optimal fault dip angle (20°) (Table 2) than that are proposed by previous studies (7°-10°). This larger dip angle may represent an average value of both flat and ramp segments. Nevertheless, our study highlights that fault geometry trades off with the inverted fault slip and biases the estimation of fault kinematics (e.g., coseismic slip, afterslip, and slip deficit/locking state), which are important for understanding the tectonics and geodynamics in Himalayan arc.

5.5. Applicability, Limitations, and Future Work

This work is designed for studying the 2015 Gorkha earthquake with the specific conditions of topographic relief and crustal heterogeneities in the central Himalayan arc. These conditions may limit the applicability of our findings to other tectonic regions. In the perspective of topographic relief, the main slip of the Gorkha event was identified beneath the Lesser Himalaya, which has a relatively gentle topographic gradient with \sim 2 km mean elevation (Figure 3c). It has been pointed out that the gradients of topographic relief can influence the predicted surface deformation and hence the earthquake source inversions (Williams & Wadge, 2000). This may explain that the topography effects are insignificant in both our forward and inverse modeling results. Studies of earthquakes with higher topographic gradients may lead to stronger topographic effects than our study. We note that we have downsampled the InSAR data to improve the signal-to-noise ratio (Lohman & Simons, 2005), resulting in coarse spatial resolution (\sim 5 km) of the data in the near field (Figure 2 and Figure S1). Guided by this InSAR data resolution and to reduce the computational cost, we use relative coarse mesh size (\sim 8 km) on the model top surface (Figure S2). This option may have dampened to a certain degree our simulated topographic effects. Higher resolution and quality data together with a finer model resolution might help to better isolate the topographic effects in future studies.

Elastic properties in the vicinity of the ruptured area feature both lateral and vertical variations (Figure 3b and Figure S3) from the regional tomographic models (Monsalve et al., 2006, 2008). These models have a

LI AND BARNHART 20 of 25



typical resolution that was determined with a permanent station network (from the Department of Mines and Geology of Nepal) and local earthquakes. There are only a few published tomographic studies available in the Gorkha area and they all have similar seismic velocity structures to our used tomographic models (e.g., Huang et al., 2009). We therefore believe that our used tomographic models have reasonably captured the first order crustal heterogeneities. Prior knowledge of different levels of velocity structure details in the Gorkha area or other regions would definitely influence the quantification of the effects of crustal heterogeneity on surface deformation (e.g., Williams & Wallace, 2018) and hence its relative importance to topographic relief, fault geometry and slip distribution. However, since our FEM inversions with the used tomographic models have explained the geodetic data within the observational errors (Root mean square < 0.2 cm LOS displacement, Figures S12 and S13), we do not think that models with more detailed velocity structures could further improve the geodetic data recovery for the Gorkha earthquake. Nevertheless, a significantly more detailed tomographic model could very well change the inferred slip distribution while fitting the data at the similar level.

Although there were geological, seismological and geodetic studies on the structure of MHT over the past several decades, its deep geometry (especially the dip and depth) is still not constrained with low uncertainty (Bilham et al., 2017; Hubbard et al., 2016). For instance, the depth uncertainties of seismologically determined earthquake location and fault geometry (e.g., Duputel et al., 2016; X. Wang et al., 2017) are typically larger than the averaged topographic relief (~2 km) associated with the Gorkha earthquake. With uncertain fault geometry, isolating the effects of topography and crustal heterogeneity in the geodetic data is more challenging as we have demonstrated in our FEM inversions. In additional to the studies with geodetic or seismological constraints, future study with multidisciplinary constraints (e.g., seismic moment release, mechanical analysis of wedge structure, and geophysical imaging) may help to narrow down the uncertainty of the fault geometry at depth and hence make it possible to quantify more detailed effects of topography and crustal heterogeneity on surface deformation and fault slip inversion.

6. Conclusions

Many previous studies have addressed the impacts of unmodeled topography and elastic structure on inversions for fault slip distributions onto a priori defined fault geometries, so in this study, we have explicitly considered the effects of unmodeled topography and elastic structure on inversions for fault geometry and location. Based on our results of three groups of forward and/or inverse modeling for the 2015 Gorkha earthquake in Central Himalayan arc involving a series of FEM models, we draw the following conclusions:

- 1. Our forward simulations confirm the impacts of topography and crustal heterogeneity on coseismic surface deformation for the Gorkha earthquake. Crustal elastic structure has more homogeneous effects in space and influences mainly the displacement magnitude, while topography has more heterogeneous effects in space and influences mainly the deformation pattern. These impacts only contribute maximally ~10% total surface displacement and the fault geometry and slip dominantly control the surface deformation for the Gorkha case
- 2. The impacts of topography and crustal heterogeneity on coseismic deformation are found to be related to fault geometry. Most profoundly, the impacts of topography depend on the fault depth. It is therefore necessary to first constrain the fault geometry, preferably by using multidisciplinary data, before including topography and heterogeneous crustal elastic structure in the earthquake source models
- 3. When inverting LOS displacements simulated by FEM models with homogeneous half-space models, including heterogeneous elastic structure in the FEM models tends to overestimate the fault dip and including topography tends to overestimate the fault depth
- 4. The horizontal displacement fields place more robust constraints on both fault dip and depth than LOS observations, regardless of the presence of topography and heterogeneous crustal elastic structure
- 5. Including topography and crustal elastic heterogeneity in the FEM inversion models with different fault geometry does not improve the geodetic data fitting for the Gorkha earthquake. It indicates that accounting for topography or crustal heterogeneity have no first-order impact on the inverted fault plane geometry for the Gorkha case

LI AND BARNHART 21 of 25



6. Inverted fault slip distribution trades off more significantly with the assumed fault geometry (especially the fault depth and dip angle) than with the topography and crustal heterogeneity for the Gorkha earth-quake. It again suggests the importance of first constraining the fault geometry before inverting the fault slip distribution

While we used the Gorkha earthquake and the topography/elastic structure associated with the region of that earthquake as our test case, our results provide a broad outline for considering epistemic uncertainties in the study of other large thrust earthquakes. Different combinations of vertical and LOS displacement observations that have different orientations relative to fault geometries and fault slip vectors will likely lead to different tradeoffs between model parameters than those that we found here. Nevertheless, our results highlight that ignoring the impacts of elastic structure and regional topographic relief systematically bias inversions for fault geometry and location, which in turn impact inversions for fault slip magnitude and distribution.

Data Availability Statement

All the data used in this work have been previously published and can be accessed at https://topex.ucsd.edu/nepal/ and <a href="ht

Acknowledgments

This work was supported by NSF grant EAR award 1645014. High-performance computational resources were provided by the University of Iowa, Iowa City. Shaoyang Li is currently a JSPS International Research Fellow. We thank Vera Schulte-Pelkum for an internal review and a discussion on the used tomography model, and Junichi Fukuda for discussion. We are grateful to the editor Thorsten Becker for handling our study, and to Charles Williams and two anonymous reviewers for constructive comments and suggestions.

References

Aagaard, B. T., Knepley, M. G., & Williams, C. A. (2013). A domain decomposition approach to implementing fault slip in finite-element models of quasi-static and dynamic crustal deformation. *Journal of Geophysical Research: Solid Earth*, 118(6), 3059–3079. https://doi. org/10.1002/jgrb.50217

Arnadóttir, T., & Segall, P. (1994). The 1989 Loma Prieta earthquake imaged from inversion of geodetic data. *Journal of Geophysical Research*, 99(B11), 21835–21855. https://doi.org/10.1029/94JB01256

Avouac, J.-P., Meng, L., Wei, S., Wang, T., & Ampuero, J.-P. (2015). Lower edge of locked Main Himalayan Thrust unzipped by the 2015 Gorkha earthquake. *Nature Geoscience*, 8, 708. https://doi.org/10.1038/ngeo2518

Barnhart, W. D., Brengman, C. M., Li, S., & Peterson, K. E. (2018). Ramp-flat basement structures of the Zagros Mountains inferred from co-seismic slip and afterslip of the 2017 Mw7. 3 Darbandikhan, Iran/Iraq earthquake. Earth and Planetary Science Letters, 496, 96–107. https://doi.org/10.1016/j.epsl.2018.05.036

Barnhart, W. D., Hayes, G. P., & Wald, D. J. (2019). Global earthquake response with imaging geodesy: Recent examples from the USGS NEIC. Remote Sensing, 11(11), 1357. https://doi.org/10.3390/rs11111357

Barnhart, W. D., & Lohman, R. B. (2010). Automated fault model discretization for inversions for coseismic slip distributions. *Journal of Geophysical Research*, 115(B10). https://doi.org/10.1029/2010JB007545

Barnhart, W. D., Murray, J. R., Yun, S. H., Svarc, J. L., Samsonov, S. V., Fielding, E. J., & Milillo, P. (2015). Geodetic constraints on the 2014 M 6.0 South Napa earthquake. Seismological Research Letters, 86(2A), 335–343. https://doi.org/10.1785/0220140210

Bilham, R., Mencin, D., Bendick, R., & Bürgmann, R. (2017). Implications for elastic energy storage in the Himalaya from the Gorkha 2015 earthquake and other incomplete ruptures of the Main Himalayan Thrust. *Quaternary International*, 462, 3–21. https://doi.org/10.1016/j.quaint.2016.09.055

Bürgmann, R., & Dresen, G. (2008). Rheology of the lower crust and upper mantle: Evidence from rock mechanics, geodesy, and field observations. *Annual Review of Earth and Planetary Sciences*, 36, 531–567. https://doi.org/10.1146/annurev.earth.36.031207.124326

Bürgmann, R., & Thatcher, W. (2013). Space geodesy: A revolution in crustal deformation measurements of tectonic processes. In M. E. Bickford (Ed.), *The web of geological advances, impacts and interactions* (pp. 397–430). Boulder, CO: Geological Society of America. https://doi.org/10.1130/2013.2500(12)

Clarke, P. J., Paradissis, D., Briole, P., England, P. C., Parsons, B. E., Billiris, H., & Ruegg, J. C. (1997). Geodetic investigation of the 13 May 1995 Kozani-Grevena (Greece) earthquake. *Geophysical Research Letters*, 24(6), 707–710. https://doi.org/10.1029/97GL00430

Crameri, F. (2018). Geodynamic diagnostics, scientific visualisation and StagLab 3.0 [Data set]. Geoscientific Model Development, 11(6), 2541–2562. https://doi.org/10.5194/gmd-11-2541-2018

Duputel, Z., Agram, P. S., Simons, M., Minson, S. E., & Beck, J. L. (2014). Accounting for prediction uncertainty when inferring subsurface fault slip. *Geophysical Journal International*, 197(1), 464–482. https://doi.org/10.1093/gji/ggt517

Duputel, Z., Vergne, J., Rivera, L., Wittlinger, G., Farra, V., & Hetényi, G. (2016). The 2015 Gorkha earthquake: A large event illuminating the Main Himalayan Thrust fault. *Geophysical Research Letters*, 43(6), 2517–2525. https://doi.org/10.1002/2016GL068083

Elliott, J. R., Jolivet, R., González, P. J., Avouac, J. P., Hollingsworth, J., Searle, M. P., & Stevens, V. L. (2016). Himalayan megathrust geometry and relation to topography revealed by the Gorkha earthquake. *Nature Geoscience*, 9, 174. https://doi.org/10.1038/ngeo2623

Fialko, Y. (2004). Probing the mechanical properties of seismically active crust with space geodesy: Study of the coseismic deformation due to the 1992 Mw7. 3 Landers (southern California) earthquake. *Journal of Geophysical Research*, 109(B3). https://doi.org/10.1029/2003JB002756

Fialko, Y. (2006). Interseismic strain accumulation and the earthquake potential on the southern San Andreas fault system. *Nature*, 441(7096), 968. https://doi.org/10.1038/nature04797

LI AND BARNHART 22 of 25



- Freed, A. M., Hashima, A., Becker, T. W., Okaya, D. A., Sato, H., & Hatanaka, Y. (2017). Resolving depth-dependent subduction zone viscosity and afterslip from postseismic displacements following the 2011 Tohoku-oki, Japan earthquake. Earth and Planetary Science Letters, 459, 279–290. https://doi.org/10.1016/j.epsl.2016.11.040
- Fukahata, Y., & Wright, T. J. (2008). A non-linear geodetic data inversion using ABIC for slip distribution on a fault with an unknown dip angle. *Geophysical Journal International*, 173(2), 353–364. https://doi.org/10.1111/j.1365-246X.2007.03713.x
- Fukuda, J. I., & Johnson, K. M. (2008). A fully Bayesian inversion for spatial distribution of fault slip with objective smoothing. *Bulletin of the Seismological Society of America*, 98(3), 1128–1146. https://doi.org/10.1785/0120070194
- Funning, G. J., Parsons, B., & Wright, T. J. (2007). Fault slip in the 1997 Manyi, Tibet earthquake from linear elastic modelling of InSAR displacements. *Geophysical Journal International*, 169(3), 988–1008. https://doi.org/10.1111/j.1365-246X.2006.03318.x
- Harris, R. A., Barall, M., Aagaard, B., Ma, S., Roten, D., Olsen, K., & Ampuero, J. P. (2018). A suite of exercises for verifying dynamic earth-quake rupture codes. Seismological Research Letters, 89(3), 1146–1162. https://doi.org/10.1785/0220170222
- Hashima, A., Becker, T. W., Freed, A. M., Sato, H., & Okaya, D. A. (2016). Coseismic deformation due to the 2011 Tohoku-oki earthquake: Influence of 3-D elastic structure around Japan. Earth, Planets and Space, 68(1), 1–15. https://doi.org/10.1186/s40623-016-0535-9
- Hayes, G. P., Briggs, R. W., Barnhart, W. D., Yeck, W. L., McNamara, D. E., Wald, D. J., & Jaiswal, K. S. (2015). Rapid characterization of the 2015 M w 7.8 Gorkha, Nepal, earthquake sequence and its seismotectonic context. Seismological Research Letters, 86(6), 1557–1567. https://doi.org/10.1785/0220150145
- Hearn, E. H. & Burgmann, R. (2005). The effect of elastic layering on inversions of GPS data for coseismic slip and resulting stress changes: Strike-slip earthquakes. *Bulletin of the Seismological Society of America*, 95(5), 1637–1653. https://doi.org/10.1785/0120040158
- Hsu, Y. J., Simons, M., Williams, C., & Casarotti, E. (2011). Three-dimensional FEM derived elastic Green's functions for the coseismic deformation of the 2005 Mw 8.7 Nias-Simeulue, Sumatra earthquake. *Geochemistry, Geophysics, Geosystems*, 12(7). https://doi.org/10.1029/2011GC003553
- Huang, G. C. D., Wu, F. T., Roecker, S. W., & Sheehan, A. F. (2009). Lithospheric structure of the central Himalaya from 3-D tomographic imaging. *Tectonophysics*, 475(3-4), 524-543. https://doi.org/10.1016/j.tecto.2009.06.023
- Hubbard, J., Almeida, R., Foster, A., Sapkota, S. N., Bürgi, P., & Tapponnier, P. (2016). Structural segmentation controlled the 2015 Mw 7.8 Gorkha earthquake rupture in Nepal. *Geology*, 44(8), 639–642. https://doi.org/10.1130/G38077.1
- Ingleby, T., Wright, T. J., Hooper, A., Craig, T. J., & Elliott, J. R. (2020). Constraints on the geometry and frictional properties of the Main Himalayan Thrust using coseismic, postseismic, and interseismic deformation in Nepal. *Journal of Geophysical Research: Solid Earth*, 125(2). https://doi.org/10.1029/2019JB019201
- Itoh, Y., Wang, K., Nishimura, T., & He, J. (2019). Compliant volcanic arc and backarc crust in southern Kurile suggested by interseismic geodetic deformation. *Geophysical Research Letters*, 46(21), 11790–11798. https://doi.org/10.1029/2019GL084656
- Kyriakopoulos, C., Masterlark, T., Stramondo, S., Chini, M., & Bignami, C. (2013). Coseismic slip distribution for the Mw 9 2011 To-hoku-Oki earthquake derived from 3-D FE modeling. *Journal of Geophysical Research: Solid Earth*, 118(7), 3837–3847. https://doi.org/10.1002/jgrb.50265
- Langer, L., Gharti, H. N., & Tromp, J. (2019). Impact of topography and three-dimensional heterogeneity on coseismic deformation. Geo-physical Journal International, 217(2), 866–878. https://doi.org/10.1093/gji/ggz060
- Langer, L., Ragon, T., Sladen, A., & Tromp, J. (2020). Impact of topography on earthquake static slip inversions. *Tectonophysics*. https://doi.org/10.1016/j.tecto.2020.228566
- Li, S., Barnhart, W. D., & Moreno, M. (2018). Geometrical and frictional effects on incomplete rupture and shallow slip deficit in ramp-flat structures. *Geophysical Research Letters*, 45(17), 8949–8957. https://doi.org/10.1029/2018GL079185
- Li, S., Bedford, J., Moreno, M., Barnhart, W. D., Rosenau, M., & Oncken, O. (2018). Spatiotemporal variation of mantle viscosity and the presence of cratonic mantle inferred from 8 years of postseismic deformation following the 2010 Maule, Chile, earthquake. *Geochemistry, Geophysics, Geosystems*, 19(9), 3272–3285. https://doi.org/10.1029/2018GC007645
- Li, S., Moreno, M., Bedford, J., Rosenau, M., & Oncken, O. (2015). Revisiting viscoelastic effects on interseismic deformation and locking degree: A case study of the Peru-North Chile subduction zone. *Journal of Geophysical Research: Solid Earth*, 120(6), 4522–4538. https://doi.org/10.1002/2015JB011903
- Lindsey, E. O., Natsuaki, R., Xu, X., Shimada, M., Hashimoto, M., Melgar, D., & Sandwell, D. T. (2015). Line-of-sight displacement from ALOS-2 interferometry: Mw 7.8 Gorkha Earthquake and Mw 7.3 aftershock. *Geophysical Research Letters*, 42(16), 6655–6661. https://doi.org/10.1002/2015GL065385
- Li, S., Wang, K., Wang, Y., Jiang, Y., & Dosso, S. E. (2018). Geodetically inferred locking state of the Cascadia megathrust based on a viscoelastic Earth model. *Journal of Geophysical Research: Solid Earth*, 123(9), 8056–8072. https://doi.org/10.1029/2018JB015620
- Lohman, R. B., & Simons, M. (2005). Some thoughts on the use of InSAR data to constrain models of surface deformation: Noise structure and data downsampling. *Geochemistry, Geophysics, Geosystems*, 6(1). https://doi.org/10.1029/2004GC000841
- Masterlark, T. (2003). Finite element model predictions of static deformation from dislocation sources in a subduction zone: Sensitivities to homogeneous, isotropic, Poisson-solid, and half-space assumptions. *Journal of Geophysical Research*, 108(B11). https://doi.org/10.1029/2002JB002296
- Masterlark, T., DeMets, C., Wang, H. F., Sanchez, O., & Stock, J. (2001). Homogeneous vs heterogeneous subduction zone models: Coseismic and postseismic deformation. *Geophysical Research Letters*, 28(21), 4047–4050. https://doi.org/10.1029/2001GL013612
- McNamara, D. E., Yeck, W. L., Barnhart, W. D., Schulte-Pelkum, V., Bergman, E., Adhikari, L. B., & Earle, P. S. (2017). Source modeling of the 2015 Mw 7.8 Nepal (Gorkha) earthquake sequence: Implications for geodynamics and earthquake hazards. *Tectonophysics*, 714, 21–30. https://doi.org/10.1016/j.tecto.2016.08.004
- Mencin, D., Bendick, R., Upreti, B. N., Adhikari, D. P., Gajurel, A. P., Bhattarai, R. R., & Bilham, R. (2016). Himalayan strain reservoir inferred from limited afterslip following the Gorkha earthquake. *Nature Geoscience*, 9, 533. https://doi.org/10.1038/ngeo2734
- Monsalve, G., Sheehan, A., Rowe, C., & Rajaure, S. (2008). Seismic structure of the crust and the upper mantle beneath the Himalayas: Evidence for eclogitization of lower crustal rocks in the Indian Plate. *Journal of Geophysical Research*, 113(B8). https://doi.org/10.1029/2007JB005424
- Monsalve, G., Sheehan, A., Schulte-Pelkum, V., Rajaure, S., Pandey, M. R., & Wu, F. (2006). Seismicity and one-dimensional velocity structure of the Himalayan collision zone: Earthquakes in the crust and upper mantle. *Journal of Geophysical Research*, 111(B10). https://doi.org/10.1029/2005JB004062
- Nealy, J. L., Benz, H. M., Hayes, G. P., Bergman, E. A., & Barnhart, W. D. (2017). The 2008 Wells, Nevada, earthquake sequence: Source constraints using calibrated multiple-event relocation and InSAR. *Bulletin of the Seismological Society of America*, 107(3), 1107–1117. https://doi.org/10.1785/0120160298

LI AND BARNHART 23 of 25



- Nissen, E., Ghods, A., Karasözen, E., Elliott, J. R., Barnhart, W. D., Bergman, E. A., & Abdulnaby, W. (2019). The 12 November 2017 Mw 7.3 Ezgeleh-Sarpolzahab (Iran) earthquake and active tectonics of the Lurestan arc. *Journal of Geophysical Research: Solid Earth*, 124(2), 2124–2152. https://doi.org/10.1029/2018JB016221
- Okada, Y. (1985). Surface deformation due to shear and tensile faults in a half-space. Bulletin of the Seismological Society of America, 75(4), 1135–1154.
- Pandey, M. R., Tandukar, R. P., Avouac, J. P., Lave, J., & Massot, J. P. (1995). Interseismic strain accumulation on the Himalayan crustal ramp (Nepal). Geophysical Research Letters, 22(7), 751–754. https://doi.org/10.1029/94GL02971
- Pollitz, F. F. (1996). Coseismic deformation from earthquake faulting on a layered spherical Earth. *Geophysical Journal International*, 125(1), 1–14. https://doi.org/10.1111/j.1365-246X.1996.tb06530.x
- Pollitz, F. F. (2015). Postearthquake relaxation evidence for laterally variable viscoelastic structure and water content in the Southern California mantle. *Journal of Geophysical Research: Solid Earth*, 120(4), 2672–2696. https://doi.org/10.1002/2014JB011603
- Pollitz, F. F., Wicks, C., & Thatcher, W. (2001). Mantle flow beneath a continental strike-slip fault: Postseismic deformation after the 1999 Hector Mine earthquake. Science, 293(5536), 1814–1818. https://doi.org/10.1126/science.1061361
- Qiu, Q., Moore, J. D., Barbot, S., Feng, L., & Hill, E. M. (2018). Transient rheology of the Sumatran mantle wedge revealed by a decade of great earthquakes. *Nature Communications*, 9(1), 1–13. https://doi.org/10.1038/s41467-018-03298-6
- Ragon, T., Sladen, A., & Simons, M. (2018). Accounting for uncertain fault geometry in earthquake source inversions–I: Theory and simplified application. *Geophysical Journal International*, 214(2), 1174–1190. https://doi.org/10.1093/gji/ggy187
- Reilinger, R. E., Ergintay, S., Bürgmann, R., McClusky, S., Lenk, O., Barka, A., & Aktug, B. (2000). Coseismic and postseismic fault slip for the 17 August 1999, M= 7.5, Izmit, Turkey earthquake. Science, 289(5484), 1519–1524. https://doi.org/10.1126/science.289.5484.1519
- Sambridge, M. (1999). Geophysical inversion with a neighbourhood algorithm—I. Searching a parameter space. *Geophysical Journal International*, 138(2), 479–494. https://doi.org/10.1046/j.1365-246X.1999.00876.x
- Sato, K., Baba, T., Hori, T., Hyodo, M., & Kaneda, Y. (2010). Afterslip distribution following the 2003 Tokachioki earthquake: An estimation based on the Green's functions for an inhomogeneous elastic space with subsurface structure. *Earth, Planets and Space*, 62(12), 923–932. https://doi.org/10.5047/eps.2010.11.007
- Sato, K., Minagawa, N., Hyodo, M., Baba, T., Hori, T., & Kaneda, Y. (2007). Effect of elastic inhomogeneity on the surface displacements in the northeastern Japan: Based on three-dimensional numerical modeling. *Earth, Planets and Space*, 59(10), 1083–1093. https://doi.org/10.1186/BF03352051
- Schulte-Pelkum, V., Monsalve, G., Sheehan, A., Pandey, M. R., Sapkota, S., Bilham, R., & Wu, F. (2005). Imaging the Indian subcontinent beneath the Himalaya. *Nature*, 435(7046), 1222. https://doi.org/10.1038/nature03678
- Simons, M., Fialko, Y., & Rivera, L. (2002). Coseismic deformation from the 1999 M w 7.1 Hector Mine, California, earthquake as inferred from InSAR and GPS observations. *Bulletin of the Seismological Society of America*, 92(4), 1390–1402. https://doi.org/10.1785/0120000933
- Smith, W. H., & Sandwell, D. T. (1997). Global sea floor topography from satellite altimetry and ship depth soundings. *Science*, 277(5334), 1956–1962. https://doi.org/10.1126/science.277.5334.1956
- Stramondo, S., Moro, M., Tolomei, C., Cinti, F. R., & Doumaz, F. (2005). InSAR surface displacement field and fault modelling for the 2003 Bam earthquake (southeastern Iran). *Journal of Geodynamics*, 40(2–3), 347–353. https://doi.org/10.1016/j.jog.2005.07.013
- Sun, J., Johnson, K. M., Cao, Z., Shen, Z., Bürgmann, R., & Xu, X. (2011). Mechanical constraints on inversion of coseismic geodetic data for fault slip and geometry: Example from InSAR observation of the 6 October 2008 Mw 6.3 Dangxiong-Yangyi (Tibet) earthquake. *Journal of Geophysical Research*, 116(B1). https://doi.org/10.1029/2010JB007849
- Sun, T., & Wang, K. (2015). Viscoelastic relaxation following subduction earthquakes and its effects on afterslip determination. *Journal of Geophysical Research: Solid Earth*, 120(2), 1329–1344. https://doi.org/10.1002/2014JB011707
- Tung, S., Katzenstein, K., Masterlark, T., Lei, J., Wauthier, C., & Petley, D. (2019). Sensitivities of geodetic source analyses to elastic crust heterogeneity constrained by seismic tomography for the 2017 Mw 6.5 Jiuzhaigou, China, earthquake. Seismological Research Letters, 90(5), 1859–1875. https://doi.org/10.1785/0220180272
- Tung, S., & Masterlark, T. (2016). Coseismic slip distribution of the 2015 Mw7. 8 Gorkha, Nepal, earthquake from joint inversion of GPS and InSAR data for slip within a 3-D heterogeneous Domain. *Journal of Geophysical Research: Solid Earth*, 121(5), 3479–3503. https://doi.org/10.1002/2015JB012497
- Tung, S., & Masterlark, T. (2018). Resolving source geometry of the 24 August 2016 Amatrice, central Italy, earthquake from InSAR data and 3D finite-element modeling. *Bulletin of the Seismological Society of America*, 108(2), 553–572. https://doi.org/10.1785/0120170139
- Wang, K., & Fialko, Y. (2018). Observations and modeling of coseismic and postseismic deformation due to the 2015 Mw 7.8 Gorkha (Nepal) earthquake. *Journal of Geophysical Research: Solid Earth*, 123(1), 761–779. https://doi.org/10.1002/2017JB014620
- Wang, K., Hu, Y., & He, J. (2012). Deformation cycles of subduction earthquakes in a viscoelastic Earth. *Nature*, 484(7394), 327–332. https://doi.org/10.1038/nature11032
- Wang, R., Martín, F. L., & Roth, F. (2003). Computation of deformation induced by earthquakes in a multi-layered elastic crust—FORTRAN programs EDGRN/EDCMP. Computers & Geosciences, 29(2), 195–207. https://doi.org/10.1016/S0098-3004(02)00111-5
- Wang, X., Wei, S., & Wu, W. (2017). Double-ramp on the Main Himalayan Thrust revealed by broadband waveform modeling of the 2015 Gorkha earthquake sequence. Earth and Planetary Science Letters, 473, 83–93. https://doi.org/10.1016/j.epsl.2017.05.032
- Wessel, P., & Smith, W. H. F. (1998). New, improved version of the Generic Mapping Tools released [Data set]. Eos, Transactions American Geophysical Union, 79, 579. https://doi.org/10.1029/98EO00426
- Williamson, A. L., & Newman, A. V. (2018). Limitations of the resolvability of finite-fault models using static land-based geodesy and openocean tsunami waveforms. *Journal of Geophysical Research: Solid Earth*, 123(10), 9033–9048. https://doi.org/10.1029/2018JB016091
- Williams, C. A., & Wadge, G. (1998). The effects of topography on magma chamber deformation models: Application to Mt. Etna and radar interferometry. *Geophysical Research Letters*, 25(10), 1549–1552. https://doi.org/10.1029/98GL01136
- Williams, C. A., & Wadge, G. (2000). An accurate and efficient method for including the effects of topography in three-dimensional elastic models of ground deformation with applications to radar interferometry. *Journal of Geophysical Research*, 105(B4), 8103–8120. https://doi.org/10.1029/1999JB900307
- Williams, C. A., & Wallace, L. M. (2015). Effects of material property variations on slip estimates for subduction interface slow-slip events. Geophysical Research Letters, 42(4), 1113–1121. https://doi.org/10.1002/2014GL062505
- Williams, C. A., & Wallace, L. M. (2018). The impact of realistic elastic properties on inversions of shallow subduction interface slow slip events using seafloor geodetic data. *Geophysical Research Letters*, 45(15), 7462–7470. https://doi.org/10.1029/2018GL078042
- Wright, T. J., Parsons, B., England, P. C., & Fielding, E. J. (2004). InSAR observations of low slip rates on the major faults of western Tibet. Science, 305(5681), 236–239. https://doi.org/10.1126/science.1096388

LI AND BARNHART 24 of 25



10.1029/2020GC009413



Wright, T. J., Parsons, B. E., Jackson, J. A., Haynes, M., Fielding, E. J., England, P. C., & Clarke, P. J. (1999). Source parameters of the 1 October 1995 Dinar (Turkey) earthquake from SAR interferometry and seismic bodywave modelling. Earth and Planetary Science Letters, 172(1–2), 23–37. https://doi.org/10.1016/S0012-821X(99)00186-7

Zhang, C., Masterlark, T., Tan, K., Wang, Q., Qiao, X., & Yang, S. (2019). The influence of topography and crustal heterogeneity on coseismic deformation of the 2008 Mw7. 9 Wenchuan Earthquake, China. *Tectonophysics*, 228305. https://doi.org/10.1016/j.tecto.2019.228305 Zhao, B., Bürgmann, R., Wang, D., Tan, K., Du, R., & Zhang, R. (2017). Dominant controls of downdip afterslip and viscous relaxation on the postseismic displacements following the Mw7. 9 Gorkha, Nepal, earthquake. *Journal of Geophysical Research: Solid Earth*, 122(10), 8376–8401. https://doi.org/10.1002/2017JB014366

LI AND BARNHART 25 of 25